POLITECNICO DI TORINO

Department of Engineering

Master Degree in Mechanical Engineering

Master Degree Thesis

Influence of non-metallic inclusion and time varying residual stress on rolling contact fatigue of bearing balls

Tutor:
Prof. Paolo Matteis
Prof. Raffaella Sesana

Candidate:
Omid Tahmasebi

Academic Year 2019/2020

Abstract

The goal of this study is to investigate the effect of inclusions on the early fatigue life of rolling bodies. In order to do this, a numerical method was considered, and its results were correlated with experimental results obtained, investigating whether a stress threshold could be defined, to be related to the life bearing requirements. Nowadays rolling element bearings are part of almost all machinery drivetrains with rotary motion. These components have a two major role of supporting load and enabling rotational motion with low friction loss. If the bearing installation is properly done and operation is under an appropriate load, temperature, and speed, then the dominant mode of failure will be due to material fatigue which is commonly referred to as rolling contact fatigue (RCF).

RCF has different modes that differ from one another in terms of driving factor and crack location. The most frequent types of RCF are surface pitting and subsurface initiated spalling. in the past decades particularly with the vacuum degassing and arc remelting processes steel cleanliness has been significantly improved. because of the manufacturing process there will be some impurities and non-metallic inclusions. These inhomogeneities have crucial effect on the fatigue performances, as the damage evolution of the rolling elements of bearings is highly affected by the micro-inclusion presence in the steel matrices. This study is focused on the AISI 52100 (100Cr6), which is the main steel used in bearings production.

stress concentration around Non-metallic inclusions originate cracks which lead to failure. composition, dimension, configuration and distribution of inclusions were considered so their effect on the fatigue life changes will be observed. Residual stresses have been measured using an X-ray diffractometer to investigate the effect of compressive residual stress changes during time so their effect on fatigue life changes can be illustrated. the initial residual stress drop at early life span was considered as the initiation of crack cause and its effect on the increase of the stresses around the non-metallic inclusions are evaluated by MATLAB code [16] based on the Eshelby solution. this stress is used to find stress threshold parameter. a good matching of the data is observed between numerical and experimental results (balls and specimen from test rigs and RBF test machine).

Content

Chapter 1

1.Introduction

Tsubaki Nakashima Co., Ltd. is one of the main manufacturers in the field of bearing and precision products worldwide. It is specialized in the production of rolling contact elements which can be made of different shape (balls or cylinder) or material (steel or ceramic). Pinerolo plant, where this study was carried out, is focused on high precision steel balls production.

Bearing is as a part of a machine that allows one part to rotate or move in contact with another part with as little friction as possible. Additional functions include the transmission of loads and enabling the accurate location of components. [1]

A wide variety of bearing designs exists to allow the demands of the application to be correctly met for maximum efficiency, reliability, durability and performance.
Bearings are composed of different elements: cylinders or balls as rolling elements and external and internal rings, which form the raceways. Also, the lubrication between the

parts is very important. Fatigue life performances of the rolling elements have a key role to prevent premature failures of the bearings during working operations. For this reason, it is important to understand how the micro-inclusions affect the life of the balls and consequently of the bearing. It is now been clearly established that fatigue resistance correlates strongly with steel cleanliness. However, inclusions are inevitably present in steels, they cannot be eliminated in the steelmaking process, [2] therefore many technical and commercial decisions by bearing manufacturers and end users depend on information regarding steel cleanliness and its effect on predicted bearing fatigue life. The two most common types of RCF failure are surface pitting or subsurface initiated spalling. In surface pitting crack starts from surface and propagate into the material which usually results in not very deep spalls. Several factors are contributing to surface pitting, such as improper lubrication or contamination in the lubricant. On the other hand, subsurface initiated fatigue cracks occur within the material and propagate toward the surface. The initiation of the fatigue cracks in the subsurface region is attributed to the fact that the dominating shear stress introduced by the cyclic load reaches its maximum in this area. These types of fatigue failure are usually associated with microstructural alterations which can be categorized to butterfly wing formation, white etching cracks, white etching bands, dark etching region and each are going to be further discussed. These names are mainly due to the special appearance of these microstructural alterations under a microscope; however, different terminologies have been used by some researchers. The correlation between steel cleanliness and fatigue life is undeniable.

Many studies have been done to investigate the role of non-metallic inclusions in the length of RCF life. The most frequently observed inclusions can mainly be categorized into groups of aluminates, silicates, sulphides, oxides, titanium Nitride.

Its more than seven decades since the first observation of microstructural alteration under rolling contact fatigue. In 1947 Jones [3] observed the irreversible microstructural alterations below the surface of the inner raceway track, which is now called the dark etching region, and he observed that as the number of cycles and load increases, this area grows.

It has been frequently observed that matrix microstructure alters in the regions adjacent to the non-metallic inclusions. This material alteration is commonly referred to as "**Butterfly- Wings**" Butterfly wings can be identified as a pair of regions with altered microstructures around an inclusion [4]. Butterflies are the first alteration that develops in the matrix and are generated in one-thousandth of the L10 life [5]. Therefore, by considering this fact it's more reasonable to focus on butterfly generation rather than continuing the tests until spalling occurs in a life test under a low load, which can happen after 10^{11} cycles in some cases. If the load is large enough, a Dark Etching Region (DERs) appears and after that white etching bands (WEBs) and white etching cracks (WECs) also appear. This chronological order has been confirmed by [5], [6]The Two wings of a butterfly are located along a line which forms a 45° angle with the Over Rolling Direction (see fig.3.2 ORD). Becker [7] investigated microstructural changes around non-metallic inclusions. The most common way to study butterflies was destructive methods at that time. The fatigue test was interrupted and after cutting and polishing the steel was etched with Nital or some other kind of etchant. He concluded that butterfly wings consist of a distribution of ultrafine-grained ferrite (10-100 nm) and carbides. the matrix microstructure γ to ferrite and carbide was assumed to be caused by a high-stress concentration which can be due to a hard inclusion or an existing crack, Moreover, Becker noticed that normal sized M_3C spherical carbides are not inside the wings, even if they are present elsewhere in the steel matrix. Becker also noted that the butterfly wing and the crack portion of the wing grow simultaneously. The altered white microstructure of the wing is about 20% harder than the surrounding matrix. Butterflies can be full of microcracks however, they are commonly accompanied by two major cracks that are in the butterfly–matrix interface at the top of the upper wing and bottom of the lower wing.

Cracks often form in the vicinity of butterfly wings and a higher number of these cracks can be observed at the top of the upper wing and the bottom of the lower wing. Grabulov [8] observed minor secondary cracks at the opposite side of the wings as well.

Different theories have been postulated on the formation of these microstructural alterations. Furumura et al. [5] suggested that the fatigue phenomenon appearing at the first stage is due to an accumulation of plastic deformation generated at the peripheral region of the oxide inclusions. Zwirlein and Shlicht [9] suggested that the formation of DER is due to additional stress from backward and forward sliding under high compressive stress. Their conclusion was only if the stress provokes slip motions in the lattice, that is if plastic deformations occur. Also, Reduction in the amount of retained austenite could prevent the formation of DER[6].

The next microstructural alteration that appears after dark etching area's is white etching bands (chronologically speaking). This phase is ferrite, which etches white, is inclined at 30◦ to the raceway, and is located between carbon-rich discs known as lenticular carbides. During contact fatigue cycling, carbon diffuses out of the white etching band and precipitates at its edges, forming the carbides discs. [9] observed that white etching crack starts at the edge of the contact area of inner raceway and link to the surface and propagate along the over rolling direction at this section. Then going toward the contact center WECs network is extended more deeply below the dark etching area (DEA) region and suggested that this is the result of induced compressive residual stress due to volumetric expansion associated with the DEA that prevents the cracks to extend in this region. With the continuation of the cycling test, another structure appears in the altered region like the 30◦ bands but thicker, longer, shallower, and inclined at an angle of 80◦ concerning the raceway. The hardness of white bands is lower compared to the unaltered microstructure.

The carbon content in 30◦ bands is about 0.2% compared to almost 0% in the 80◦ bands. Carbon diffusion is the most accepted mechanism for the development of white etching bands [6].

WEBs usually start after the L10 life (L10 is the number of inner ring million revolutions for a survival probability of 90% of the bearings), however, WECs can occur as early as 1–10% of L10 life of the bearing which makes WECs so detrimental to bearing life [10].

[11] used X-ray tomography to estimate stress concentration around non-metallic inclusions in bearing steel 100cr6. They used X-ray tomography imaging to determine 3D morphologies of the inclusions and of the conical cavities adjacent to them which very likely were formed during the rolling process. The probability of observing such cavities is quite low with classical metallographic techniques. Then after characterizing the mechanical properties of inclusions by nano-indentation and calculating the stress concentration around inclusions, a comparison between the real 3D shape and the simplified ones and the model of Eshelby was done. The cavities around inclusion induce an anisotropic behavior of the inclusion within the contact stress field. The influence zone of the inclusion is larger when the inclusion-cavities system is perpendicular to the contact surface. Eliminating the conical cavities and not considering plasticity, as in the Eshelby model, lead to a large inconsistency between the obtained stress field and the one based on real shape.

Hanwei Fu et al. [12] studied the relationship between steel making process of 100cr6, inclusion microstructure, and RCF performance for 3 continuous casting routes. The first and third routes are having the same metallurgical process (from basic oxygen furnace (BOF) to Rurhstahl Heraeus degasser (RHD)) but with different reduction ratios during hot rolling which was 97% and 93% respectively for routes 1 and 3. For the second route, the metallurgical process was Electric arc furnace to vacuum degasser followed by a reduction ratio of 86% during hot rolling. For each route, some samples were analyzed with SEM and EDX detector and for each detected inclusion the position, size and chemical composition were recorded. Then the 3D morphologies of inclusions were obtained by the electrolytic extraction method to characterize inclusions by shape. Two RCF testing methods of flat washer and ball on rod were conducted to study the RCF life. The observation after plotting the failure probability for each route was that route 1 had the worst performance in low probability regime which assumingly was due to silicate fragmentation (because of high reduction ratio in area 97%). Grabulov [6] stated that silicate fragments should be considered as a void in RCF due to incoherent interface of them with matrix and silicate fragmentation increases the number density of these voids which would be favorable for crack nucleation. The largest size of globular oxides and TiN and correspondingly worst performance at a high probability regime was found in route 2. They suggested that early failure in bearings is due to fragmented silicate inclusions and late failure due to TiN inclusions. Observing 3D morphologies obtained from electrolytic extraction results shows that MnS inclusions have a smooth profile and therefore are less detrimental to bearing life, whereas Al2O3 and TiN have some irregularities on their surface. It is worth noticing that no microstructural alterations (WEA, DER, WEB) were found in their research which they suggested that it could be due to low RCF test temperature which was not high enough to activate effective carbon-dislocation interaction for strain-induced carbon redistribution.

A study by [13] on the role of superimposed residual compressive stresses on RCF initiation at hard and soft inclusions was done and optimized residual stresses are determined that minimize the maximum attained micro-scale von Mises stress at different depths. For the purpose of calculating desirable compressive residual stress profiles with the aim of suppressing initial micro-scale plasticity around non-metallic inclusions an analytical method was performed by author .by considering the fact that concept of a fatigue limit, defined as a stress level below which no material deterioration is expected and by assuming the existence of such a limit, a micromechanical models was developed to study how this limit would be affected by presence of inclusions, based on

Eshelby's method. In most of the studied cases, optimal compressive residual stresses which reduce the maximum von Mises stresses close to the considered inclusions were found. It should be also considered that an excessive amount of compressive residual stress can have a worsening effect on fatigue performance.

The current study explores the effect of micro-inclusions and depth dependent residual stress on fatigue life of AISI 52100 steel used in balls used as rolling elements on their early stage of crack initiation. The study can be divided into these areas:

• Fatigue test on ball bearing and raw material are made in order to get real data.

• A dedicated 3D solver implementing Eshelby model [6] was developed to estimate the stress distribution surrounding the micro-inclusion. The stresses around micro-inclusion were calculated with and without the presence of residual stress.

• The calculated stresses will be used as input for a micro-inclusion threshold estimation model to estimate the life of the ball bearing.

Chapter 2

2.Rolling Contact fatigue

The rolling contact fatigue of bearings can be defined as detachment of material (spalling) following the initiation of cracks below the contact area near subsurface alternating stress field. [14] The RCF failure mechanism is being considered when a properly mounted, lubricated bearing performing under normal load is being studied. Although In the past few decades there was a huge advance toward decreasing bearing steels impurities in production, but inclusions persist.

The most common types of RCF are surface-originated pitting and subsurface initiated spalling. In case of Surface pitting, the cracks initiate from the surface and propagate into the material due to the presence of surface distresses such as dents on the surface of the contacting bodies or improper lubrication, contaminants in the lubricant which when trapped will cause increase in the contact stress. The resulting spalls in this case are normally not so deep. If the contacting bodies are relatively smooth, then the main mode of failure is subsurface-initiated spalling. In this mode of RCF cracks start from within the material and typically near the presence of inhomogeneity or inclusion and then propagate to the surface. Subsurface RCF occurs due to a complicated orthogonal subsurface shear stress reversal phenomenon. Some of subsurface fatigue failures are associated with microstructural alterations in bearing steel. [15]

Main influencing factors on rolling contact fatigue are [1]:

- Contact pressure
- Material properties
- Lubricant properties
- Surface roughness
- Relative slip during the rotation between elements
- Microstructure
- Cleanliness condition
- Residual stress
- Retained austenite

It is worth mentioning the major differences between classical fatigue and rolling contact fatigue for better understanding the phenomenon. The state of stress in nonconformal contacts is complex and multiaxial and governed by the Hertzian contact theory and it is happening in a small volume of stressed material where development of residual stresses and localized plastic deformation along with high hydrostatic stress component existence because of non-conformal contact. Also, the planes of maximum shear stress also keep changing during a stress cycle. All being said applying the results from classical fatigue to RCF is impossible.

2.1 Hertzian contact

When two elliptical surfaces are loaded against each other a small contact area is being formed through elastic deformation leading to limiting the stresses considerably. stress field created when two bodies are pressed together into contact whilst avoiding plasticity was first introduced by Hertz at 1881.

Contact conditions:

1. Geometry:
   - two bodies in contact
   - in a non-singular point of their surfaces (regular at least to the second derivative); then (first derivatives) the common tangent plane exists
2. Material:
   - elastic, isotropic
   - no frictions, meaning only the normal stresses will be translated between the two bodies.
3. Hypothesis:
   - small contact surface (length and width small compared to curvature radii od bodies in contact)

2.1.1 Geometry of smooth, non-conforming surfaces in contact

First, we must define surface properties for body

$$z_1 = z_1(x, y)$$

$$z_1(0, 0) = 0$$

$$\frac{\partial z_1}{\partial x}(0, 0) = 0$$

$$\frac{\partial z_1}{\partial y}(0, 0) = 0$$

$$z_1 = 0 + 0 \cdot x + 0 \cdot y + \frac{1}{2}\left(\frac{\partial^2_{z_1}}{\partial x^2} x^2 + 2\frac{\partial^2_{z_1}}{\partial x \partial y} xy + \frac{\partial^2_{z_1}}{\partial y^2} y^2\right) + \cdots$$

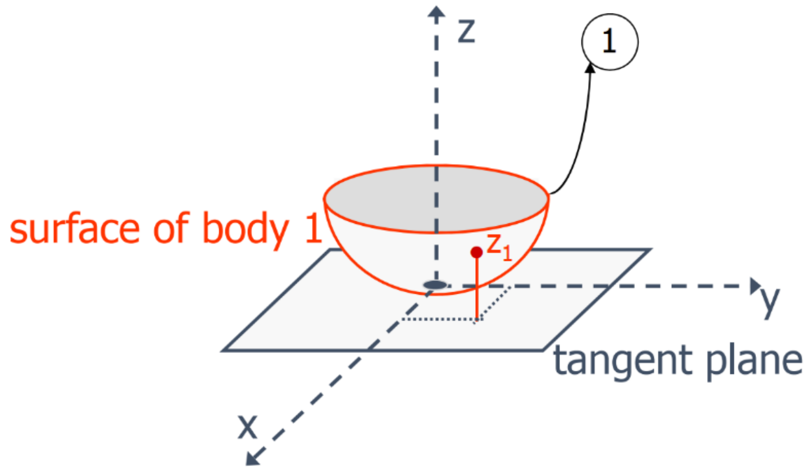

Figure 2.1- Surface of body 1

$$a_{xx} = \frac{1}{2}\frac{\partial^2_{z_1}}{\partial x^2} \rightarrow \frac{1}{2} \cdot \frac{1}{R_{xx}}$$

R_{xx} = curvature radii of the section with plane *xz*

$$a_{yy} = \frac{1}{2}\frac{\partial^2_{z1}}{\partial y^2} \rightarrow \frac{1}{2} \cdot \frac{1}{R_{yy}}$$

R_{yy} = curvature radii of the section with plane *yz*

$$a_{xy} = \frac{1}{2}\frac{\partial^2_{z_1}}{\partial_x \partial y} \quad ; \quad z_1 \cong \{x \quad y\}\begin{bmatrix} \alpha_{x_x} & \alpha_{xy} \\ \alpha_{xy} & \alpha_{yy} \end{bmatrix}\begin{pmatrix} x \\ y \end{pmatrix}$$

By defining similarly surface properties of body 2 we get:

$$\beta_{xx} = \frac{1}{2} \cdot \frac{1}{R_{xx,2}} \quad ; \quad \beta_{xy} = \frac{1}{2} \cdot \frac{1}{R_{yy,2}} \quad ; \quad z_2 = \{xy\} \begin{bmatrix} -\beta_{xx} & -\beta_{xy} \\ -\beta_{xy} & -\beta_{yy} \end{bmatrix} \begin{pmatrix} x \\ y \end{pmatrix}$$

The vertical distance between two bodies in a common reference system could be calculated as:

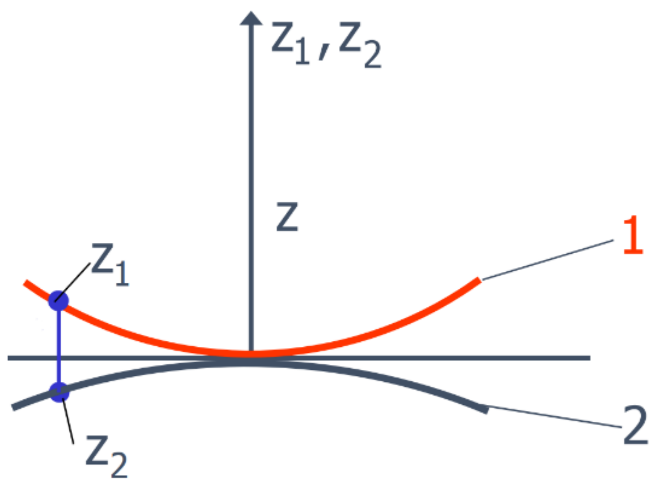

Figure 2.2-two bodies in contact

$$z_1 - z_2 = \{x \quad y\} \begin{bmatrix} \alpha_{xx} + \beta_{xx} & \alpha_{xy} + \beta_{xy} \\ \alpha_{xy} + \beta_{xy} & \alpha_{yy} + \beta_{yy} \end{bmatrix} \begin{pmatrix} X \\ y \end{pmatrix}$$

Approach of two bodies can be calculated by:

$$u_1 + u_2 = \delta - (z - z_2)$$

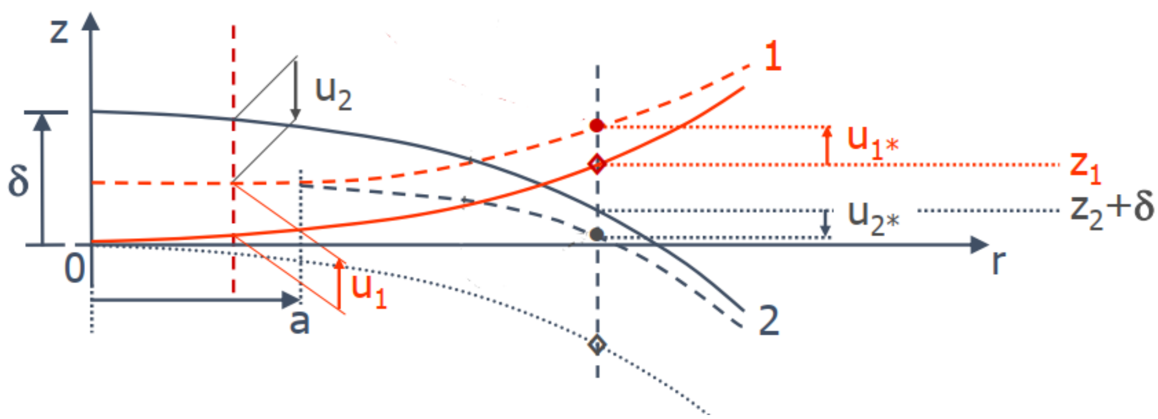

Figure 2.3-Approach of two bodies

The infinitesimal force inside each area element $dA = dx'\,dy'$ inside the contact surface at $point(x', y')$ is:

$$dF = p(x', y')dx'\,dy'$$

Which produces a displacement at arbitrary point (x, y) in the contact area. If the pressure distribution $P(x', y')$ and contact area are well known the displacement can be defined as:

$$u(x, y) = \frac{1 - v^2}{\pi E} \int \int \frac{P(x', y')}{r'} dx'\,dy'$$

Hertz found that with contact force F:

$F = \int \int p_{(x,y)} \cdot dx \cdot dy$ Then: $P = \frac{3}{2} \frac{f}{\pi ab} \cdot \sqrt{1 - \frac{x^2}{a^2} - \frac{y^2}{b^2}}$

Where a , b are the corresponding semi axis of contact area

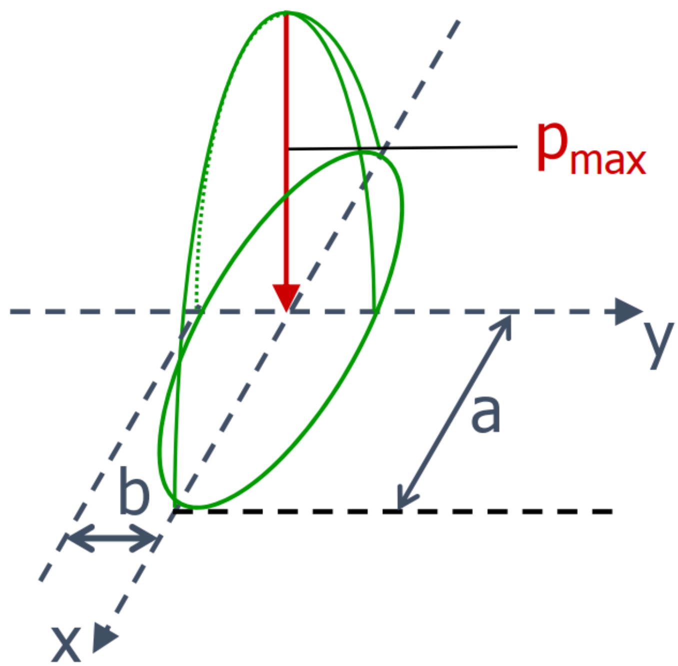

Figure 2.4-pressure distribution in contact area

2.1.2 subsurface stresses

The stress state is three dimensional and compressive. Experimental evidence shows that failure starts at points below the surface. Hertzian Contact Stresses develops Orthogonal shear-stress and Octahedral shear-stress at contact subsurface. maximum shear stress or the octahedral shear stress is the one below the center of contact the stress created just below the center of the contact. In other hand orthogonal shear stresses are created in front of and behind the contact point and they are oriented parallel and normal to the bearing raceway. And the one in front of the contact point has a negative sign with respect to the one behind the contact point. maximum shear stresses have higher magnitude of stress with respect to orthogonal shear stresses but since the later one has a higher range its contribution to the development of rolling contact fatigue is more. The range of the orthogonal shear stress is $2\tau_0$ since it reverses as the rolling contact passes a point on the raceway. The equivalent stress, often known as the von Mises stress, is given by:

$$\sigma_e = \sqrt{3\tau_e} = \frac{1}{\sqrt{2}}([\sigma_1 - \sigma_2]^2 + [\sigma_2 - \sigma_3]^2 + [\sigma_3 - \sigma_1]^2)^{\frac{1}{2}}$$

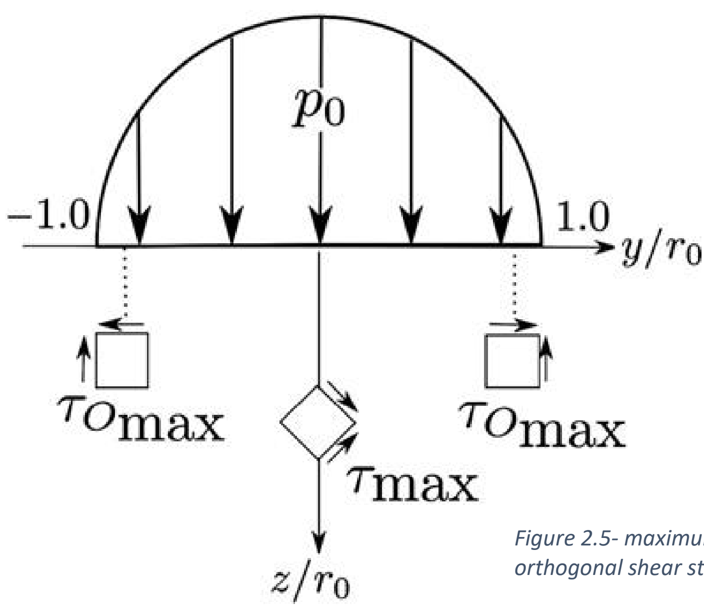

Figure 2.5- maximum shear stress and maximum orthogonal shear stress

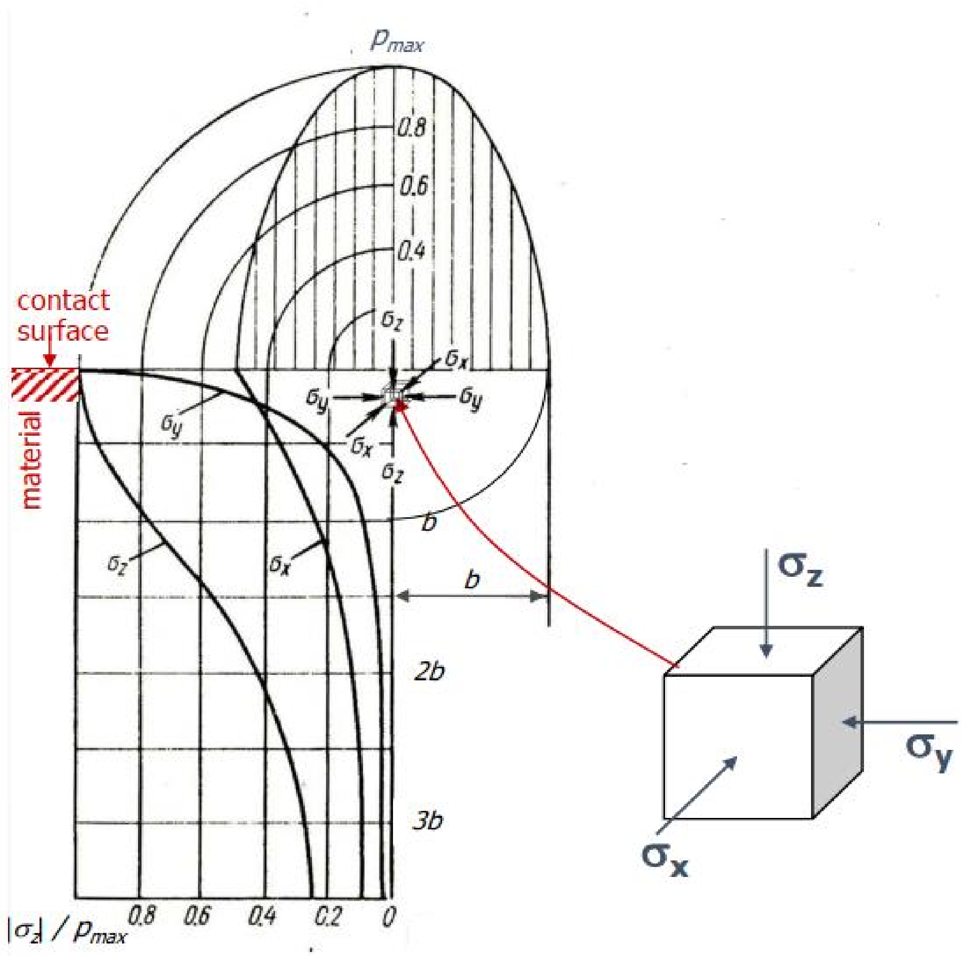

Figure 2.6-Surface and sub-surface stresses in cylindrical contact

To understand which shear stress, maximum tangential stress, von Mises stress, Tresca stress is the one that must be considered in the context of fatigue of contacting bodies many studies have been done through years [16]. by comparing the respective stress distributions against the location of maximum damage in experiments their role can be known. However, whichever shear stress is considered, the maximum occurs below the contact surface and this has significant consequences to the development of damage. Notice that the shear stress is proportional to the contact pressure p_0 but the proportionality constant will depend on the ratio of the minimum to maximum diameters of the contact.

The contact will not cause any residual stress or damage after completing the loading cycle if plastic yielding is avoided. Otherwise the induced residual stresses will combine with the existing one in yield envelope or work hardening caused from microplasticity will increase the yield strength. Another phenomena which could happen due to plasticity is increase in the contact area and reduction in contact pressure. Although these with plastic deformation, eventually deformation will continue in an elastic approach. The process is known as shakedown which will happen if all components of plastic deformation tensor become constant [17]. Micro-plastic deformation, which depends for example on localized stress concentrators, cannot be ruled out even when the when applied stresses lie within the yield envelope [18]. The shakedown limit will be different in a material which in its initial unloaded state contains residual stresses. Furthermore, a steel containing retained austenite will have a longer shakedown period than one which does not, because the progressive transformation of the austenite into martensite under the influence of stress [1]. On the other hand, the work-hardening resulting from the formation of fresh martensite leads to a smaller plastic strain prior to the achievement of the shakedown condition; this is reflected in the development of a smaller groove depth during rolling contact [1]. According to [19] the first stage of bearing operation leads to the transformation of austenite and cyclic hardening, with prolonged rolling contact causing microstructural changes that are associated with cyclic softening so that the shakedown limit is exceeded and damage accumulation accelerates.

2.2 Eshelby model

The Eshelby's inclusion problem describes the perturbed elastic displacement and stress field in an infinite homogeneous elastic body as a result of the presence of an arbitrary ellipsoidal inclusion [20]. the implementation of Eshelby's method by Meng [20] is the one used in this thesis to relate the macroscopic stresses to local stresses around non-metallic inclusions. Eshelby's solution for an inhomogeneity proves that the interior strain field which inhomogeneity embedded in an infinite matrix undergoes is uniform when subjected to a uniform eigenstrain ε_{ij}^{*} (where ε_{ij}^{*} may be plastic strains ϵ^{p}_{ij}, transformation strains ϵ^{t}_{ij} etc.) Eigenstrain refers to the stress-free deformation strain. The interior strain will be uniform and is related to the eigenstrain by:

$$\epsilon_{ij} = S_{ijkl}\epsilon^{*}_{ij},$$

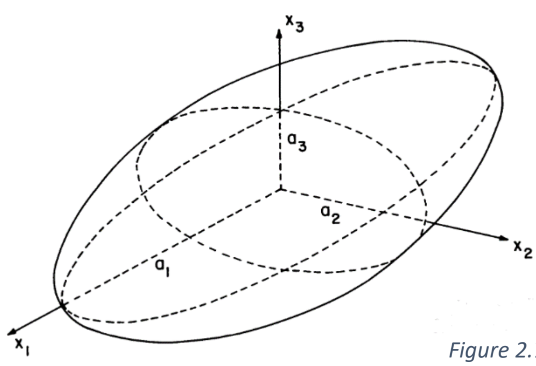

Figure 2.7-definition of the axes for an elliptical inclusion

S_{ijkl} are components of a four ranked tensor named called Eshelby tensor. For an ellipsoidal

Eshelby[20] investigated the elastic fields assuming to cut a generic region and removing it from the matrix. In this way the

region can change its shape, since it is unconstrained. Then, applying forces to the region and so restoring it to its original shape, put it back in the matrix. The applied surface tractions are integrated into a layer of body force distributed on the interface between matrix and inclusion. To complete the solution, this layer is removed by applying an equal and opposite layer of body force; the additional elastic field thus introduced is found by integration from the expression for the elastic field of a point force. It results that if the inclusion is ellipsoidal and the matrix in which it is embedded is subjected to a homogeneous load, the stress within the inclusion is uniform. This means that the elastic stress and strain don't change with the position inside the inclusion. Mura [21] defined an inclusion as a subdomain Ω in a domain *D*. The eigenstrain ε_{ij}^{*} (x) is given in Ω and zero in *D*-Ω. This is the inclusion problem, as the elastic modulus is the same for both subdomain and domain. The displacement u_j, strain ϵ_{ij}, and stress σ_{ij} are expressed by [17]:

$$u_i(x) = -C_{kjmn} \int_{\Omega} \epsilon^{*}(x') C_{ij,k}(x - x')\, dx'$$

$$\epsilon_{ij}(x) = -\frac{1}{2} \int_{\Omega} C_{klmn} \epsilon_{mn}^{*}(x') \left(G_{ij,k}(x - x') \right) + G_{jk,li}(x - x')\, dx'$$

$$\sigma(x) = -C_{ijkl} \left(\int\limits_{\Omega} C_{pqmn} \epsilon_{mn}^{*}(x') G_{kp,ql}(x - x')\, dx' + \epsilon_{kl}^{*}(x) \right)$$

- C_{ijkl} is the stiffness tensor
- G_{ij} is Green's function

Green function is given by [21]:

$$G_{ij}(\mathbf{x} - \mathbf{x}') = \frac{1}{16\pi\mu(1 - \nu)|\mathbf{x} - \mathbf{x}'|} (3 - 4\nu)\delta_{ij} + \frac{(x_i - x_i')(x_j - x_j')}{|\mathbf{x} - \mathbf{x}'|^2}$$

Given this expression of the strain for interior and exterior the inclusion, the stress field can be obtained as follows:

$$\sigma_{ij} = C_{ijkl}\, \epsilon_{kl}(x)$$

2.2.1 equivalent inclusion method

In case the elastic field we would like to evaluate is characterized by different elastic moduli and poison ratio of the matrix and subdomain, i.e., C^*_{ijkl} in Ω and C_{ijkl} in D-Ω, the problem would be different, in this case the problem is called 'the inhomogeneity problem'. the stress perturbation due to the presence of an ellipsoidal inhomogeneity of a homogeneous applied stress σ^∞_{ij}, can be determined by an inclusion problem when the eigenstrain ϵ^*_{ij} is chosen correctly. This is called the equivalent inclusion method.[20]

To solve the eigenstrain we write:

$$(\Delta C_{ijkl} S_{klmn} - C_{ijmn})\, \epsilon^*_{mn} = -\Delta C_{ijkl}\, \epsilon^\infty_{kl} - C^*_{ijkl} \epsilon^p_{kl} \,,$$

Where $\Delta C_{ijkl} = C_{ijkl} - C^*_{ijkl}$, and From $\sigma^\infty_{ij} = C_{ijkl} \epsilon^\infty_{ij}$ we can have the remote strain ϵ^∞_{ij}.

The initially subjected arbitrary eigenstrain is ϵ^p_{ij} Then we have the stress and strain fields as follows:

$$\epsilon_{ij} = \epsilon^\infty_{ij} + S_{ijmn} \epsilon^*_{mn} \,,$$

$$\sigma_{ij} = \sigma^\infty_{ij} + C_{ijkl}(S_{klmn} \epsilon^*_{mn} - \epsilon^*_{mn}) \quad \text{in } \Omega,$$

$$\epsilon_{ij}(\mathbf{x}) = \epsilon^\infty_{ij} + D_{klmn}(\mathbf{x}) \epsilon^*_{mn} \,,$$

$$\sigma_{ij}(\mathbf{x}) = \sigma^\infty_{ij} + C_{ijkl} D_{klmn}(\mathbf{x}) \epsilon^*_{mn} \,, \quad \text{for } \mathrm{X} \in D - \Omega.$$

The eigenstrain is stress free so we must subtract it from the total strain when we are calculating the interior stress. The displacement here is equivalent to the displacement perturbation caused by an inhomogeneity and does not include the displacement due to remote homogeneous stress σ^∞_{ij}

2.3 influencing factors on stress peak

The stress field under the contact area may increase due to presence of inclusion or imposed residual stresses during operation. The influence of inclusion is characterized by Eshelby model [22]. The residual stresses are measured for each depth after failure to understand the variation from the original value.

- Dimension of inclusion
- Shape of inclusion
- Depth
- Residual stress

2.3.1 dimension of inclusion

The effect of inclusion size on the stress field surrounding the inclusion is that by increasing the inclusion size the involved area subjected to stress perturbation increases. But as we can see in figure 2.7. the maximum Tresca stress peak value does not change. This result was obtained by simulation performed using the MATLAB code [22].

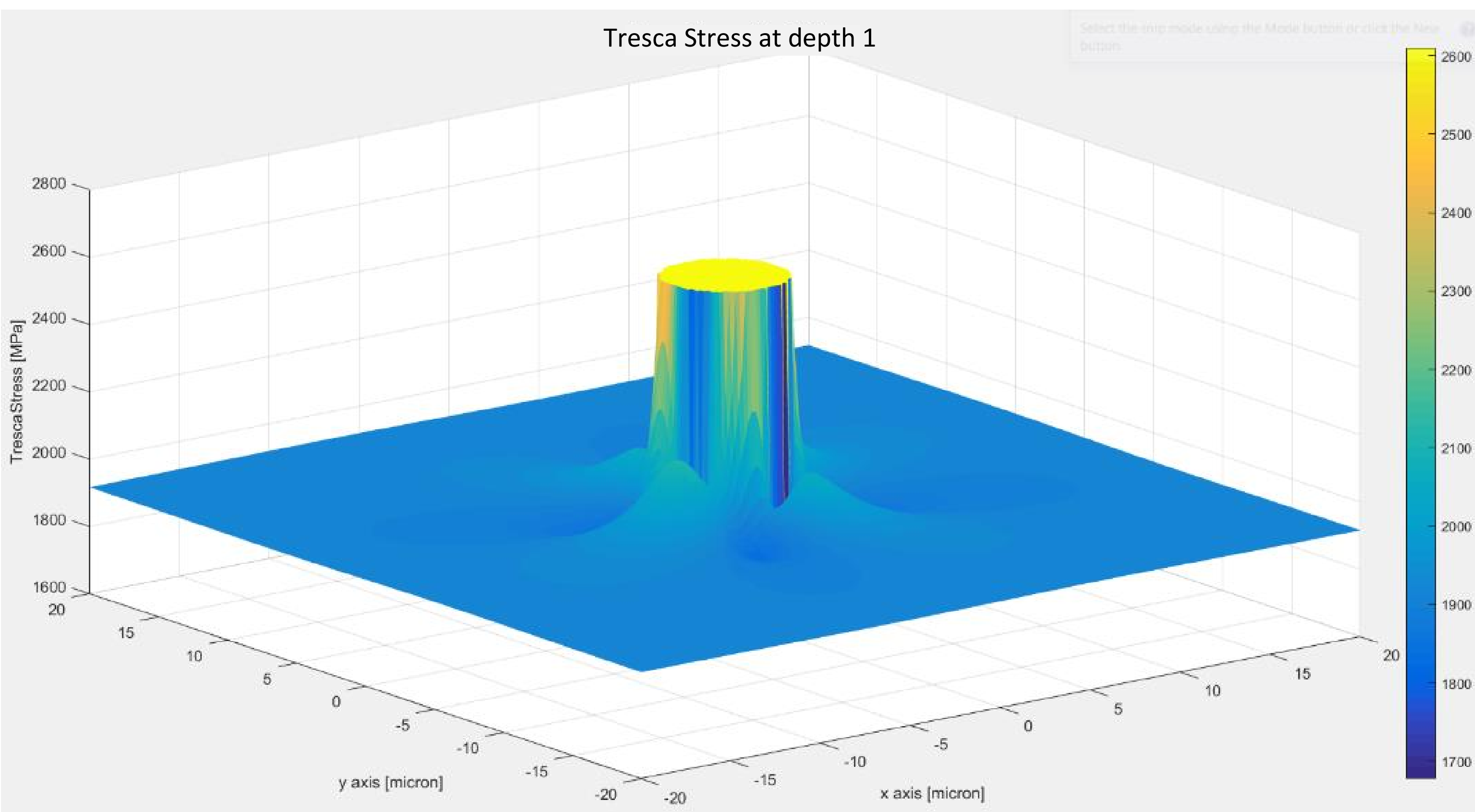

*Figure 2.8 Tresca stress for an elliptic an inclusion of size (3*3*3)*

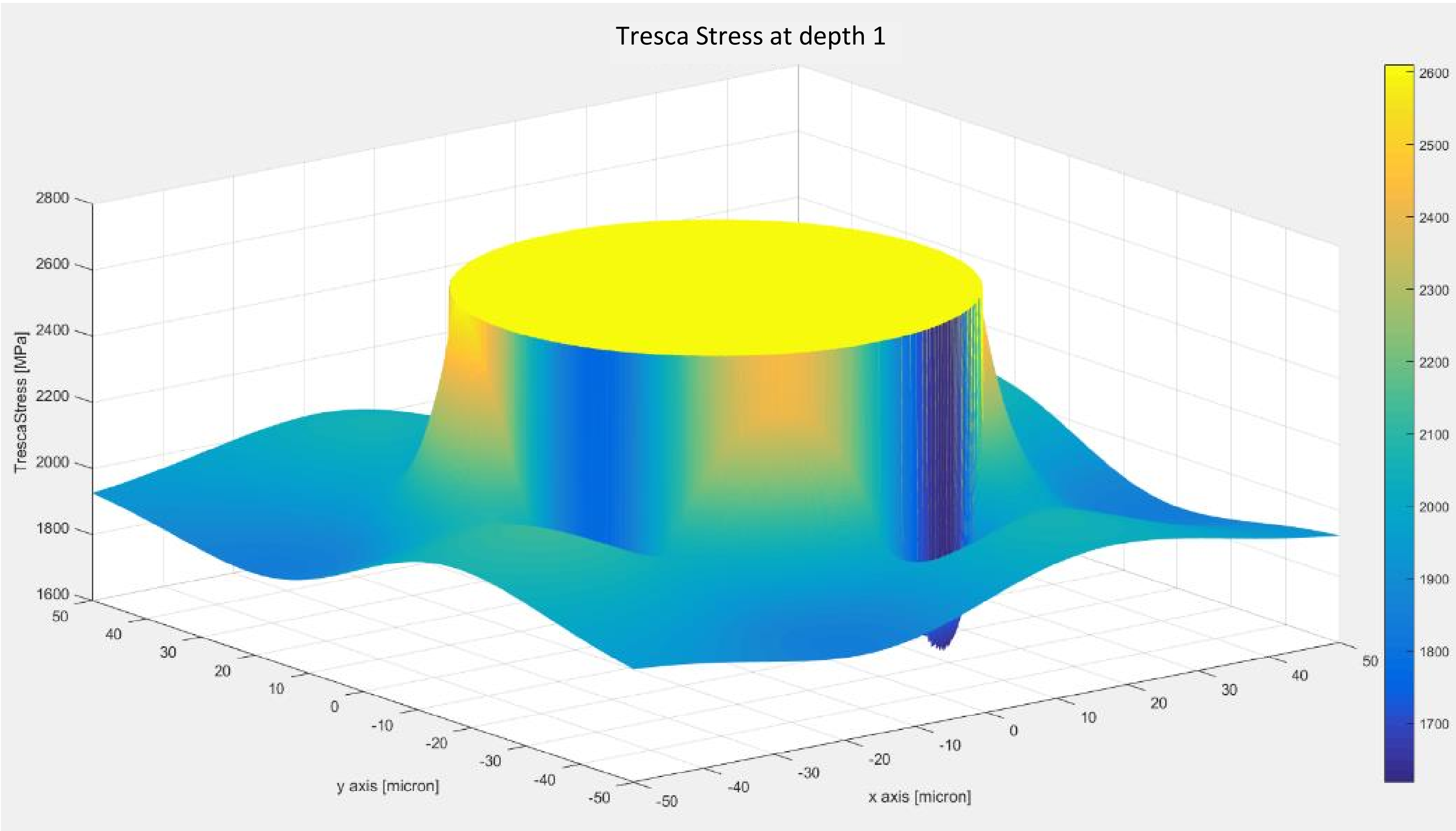

*Figure 2.9 Tresca stress for an elliptic inclusion of size (30*30*30)*

2.3.2 shape of inclusion

MATLAB code [22] was used in order to investigate the effect of shape and as we can see as the ratio between semi-minor axes and semi-major axes of elliptic inclusion increases the Tresca peak value also increases.

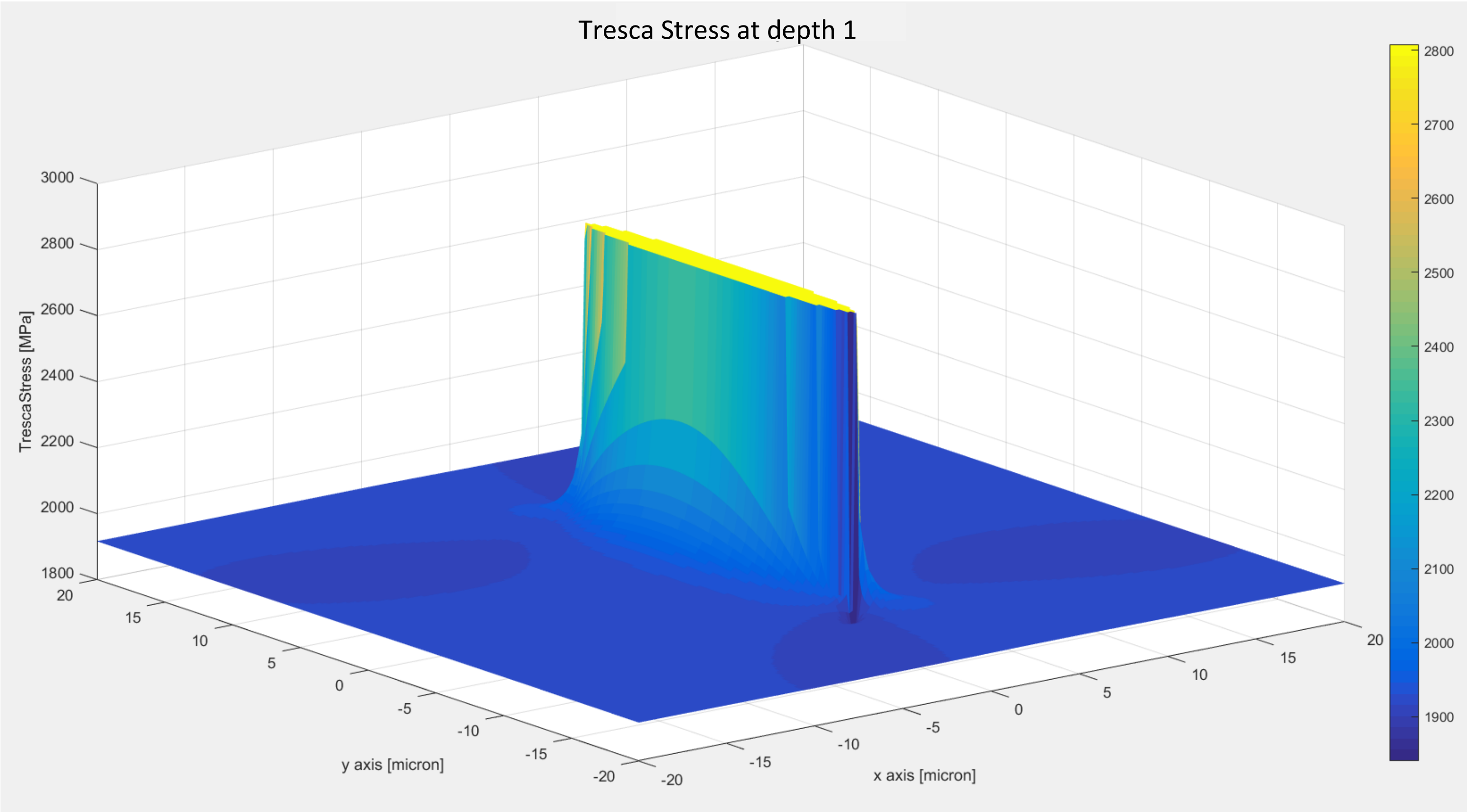

*Figure 2.10-tresca stress for an inclusion of size (1*1*10)*

2.3.3 depth

From the Hertz theory, we know that the maximum equivalent stress is located at a certain depth below the contact surface which is approximately about 0.78*(contact half width). The stress increment caused by inclusion is independent of depth but this increment is more crucial when is located at location of maximum shear stress.

2.3.4 residual stress

Comparing the residual stress profiles of new and tested balls we can observe that during operation we can see some changes in different depths of contact.

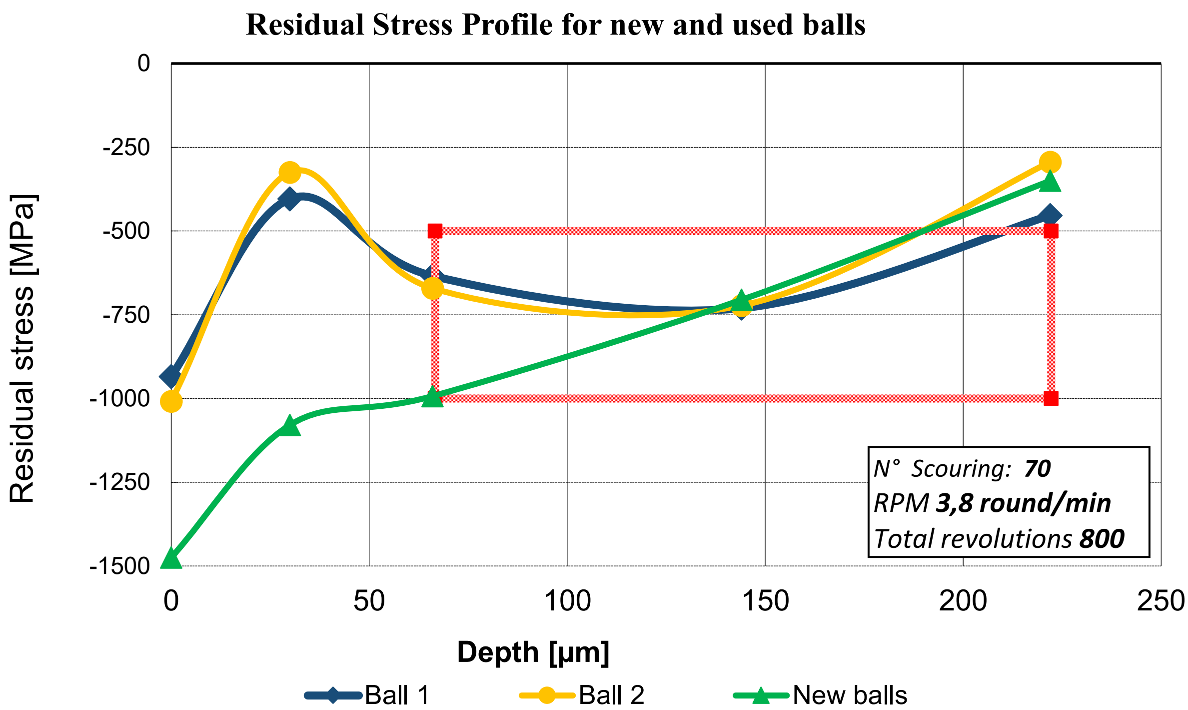

Figure 2.11-Residual stress profile for new and used balls

Chapter 3

3.Microstructural damage

Microstructural alterations in bearing steels during rolling contact cycling have been reported in the literature in the past decades. These alterations can be observed in different forms and locations and in different time span in bearing life. by using optical microscopy these changes have been reported and a terminology was created based on the differences observed between new steel and the exposed one to contact fatigue. Here we will see this change based on the chronological order of appearance of microstructural alterations.

3.1 Butterflies

butterfly wings are believed to initiate at non-metallic inclusions, voids, carbides or microcracks present in steel subjected to rolling contact cycling. they can be identified as a pair of altered microstructures around an inclusion, void etc.

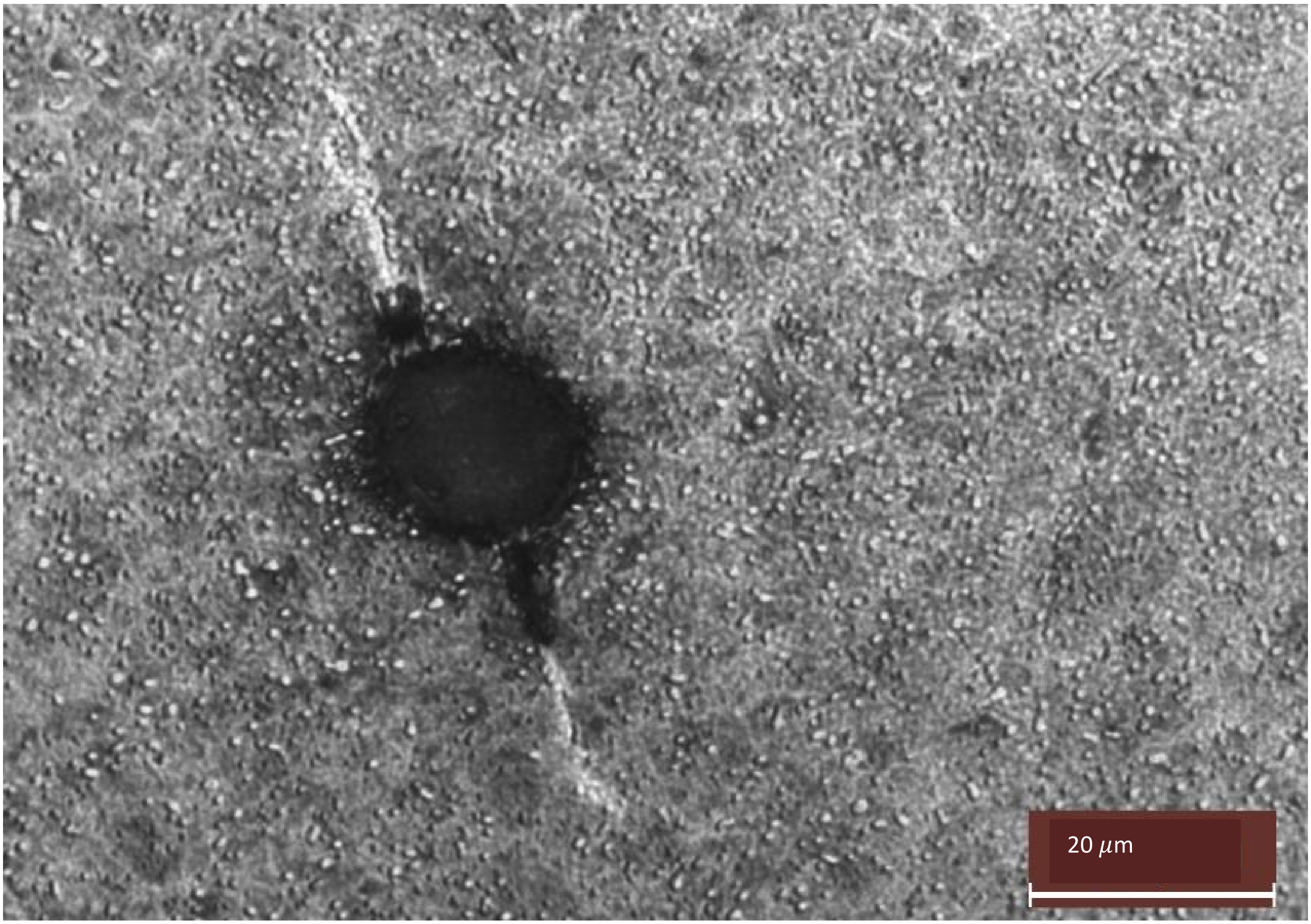

Figure 3.1- a butterfly in steel damaged by rolling contact fatigue

Change of microstructure from martensite to ferrite has been observed in the wings. The reason for the change of color in these regions is probably because of the difference in grain size (nano ferrites as small as 5-10 nm was observed inside the wings) which reflects the light differently from the etched surrounding steel. Voids are more favorable for butterfly formation followed by deboned inclusions or cracked ones. particles which are tightly fitted have the least susceptibility because the deformation in the steel at the interface between the inclusion and the matrix becomes constrained. Wings form a 45-degree angle with respect to the over rolling direction. Subsurface cracks are commonly noticed to be initiated from butterflies.

3.2 Dark etching region

we can identify DERs by their dark contrasting appearance after the material is etched with Nital and observed under the optical microscope. The effect can be observed after a few millions of cycles. The upper boundary is almost well defined while the lower region

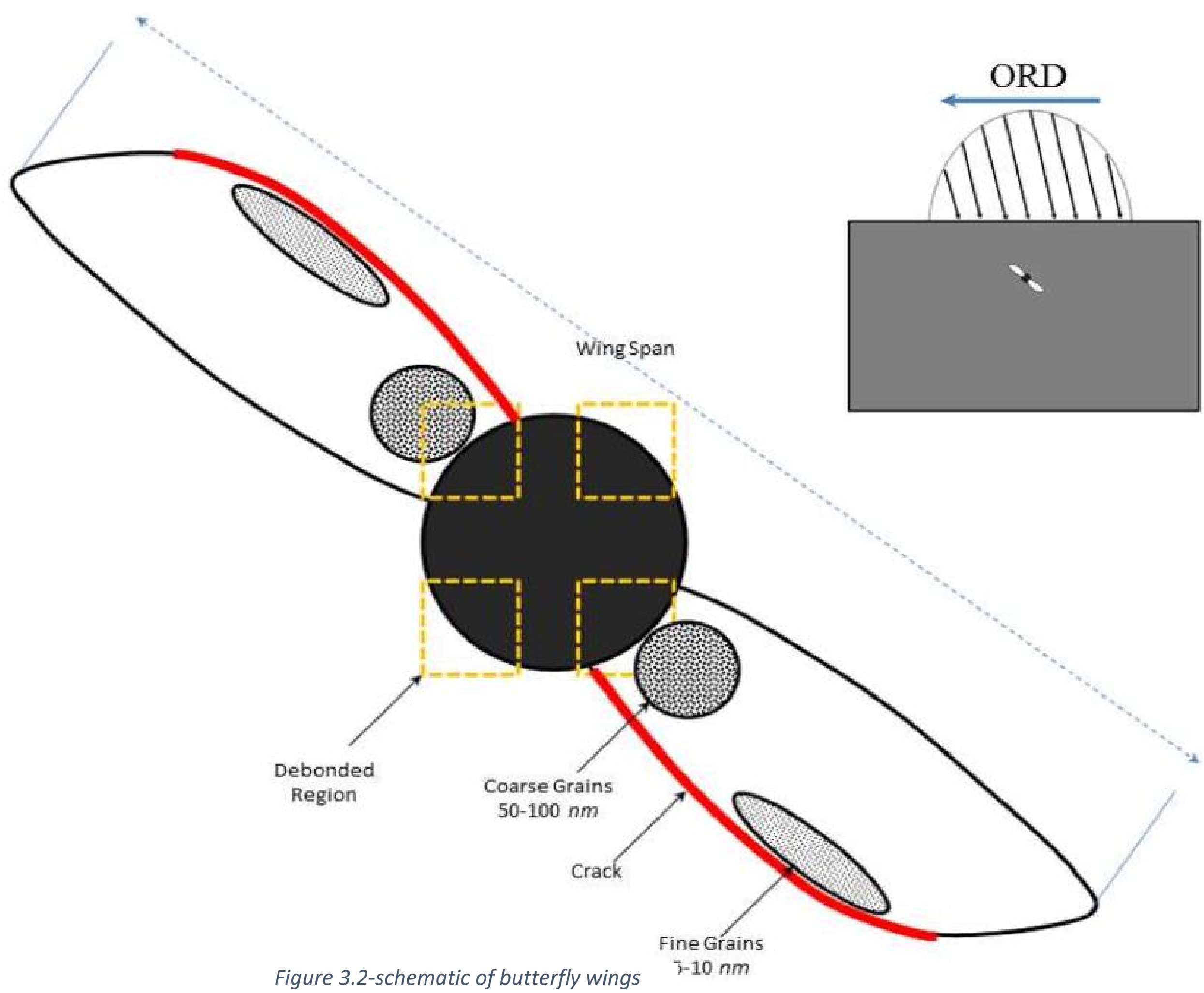

Figure 3.2-schematic of butterfly wings

is diffuse. The depth at which the DER is formed changes according to the loading conditions [23]but is normally centered in vicinity of the location of maximum shear stress. It is known that the region expands in size with increasing pressure or number of cycles.

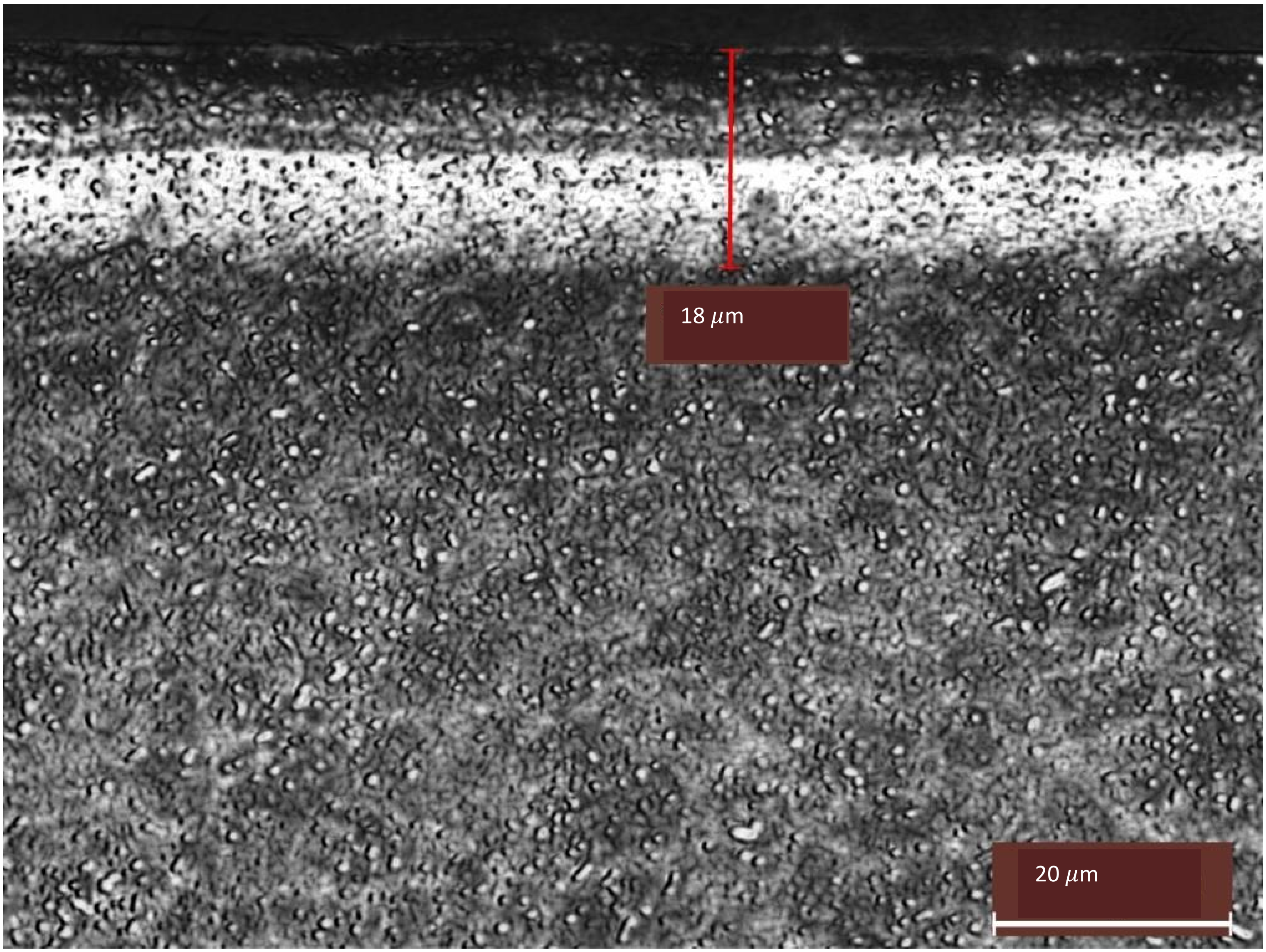

Figure 3.3-upper boundary of DER and its distance from surface under 4 MPA contact pressure

plastic strain accumulation and work-hardening was known by some scientists the main cause in the material for dark etching area formation. However, the observations are not consistent. hardness values as low as 53 HRC for DERs in surrounding matrix with 61 HRC for virgin microstructure.

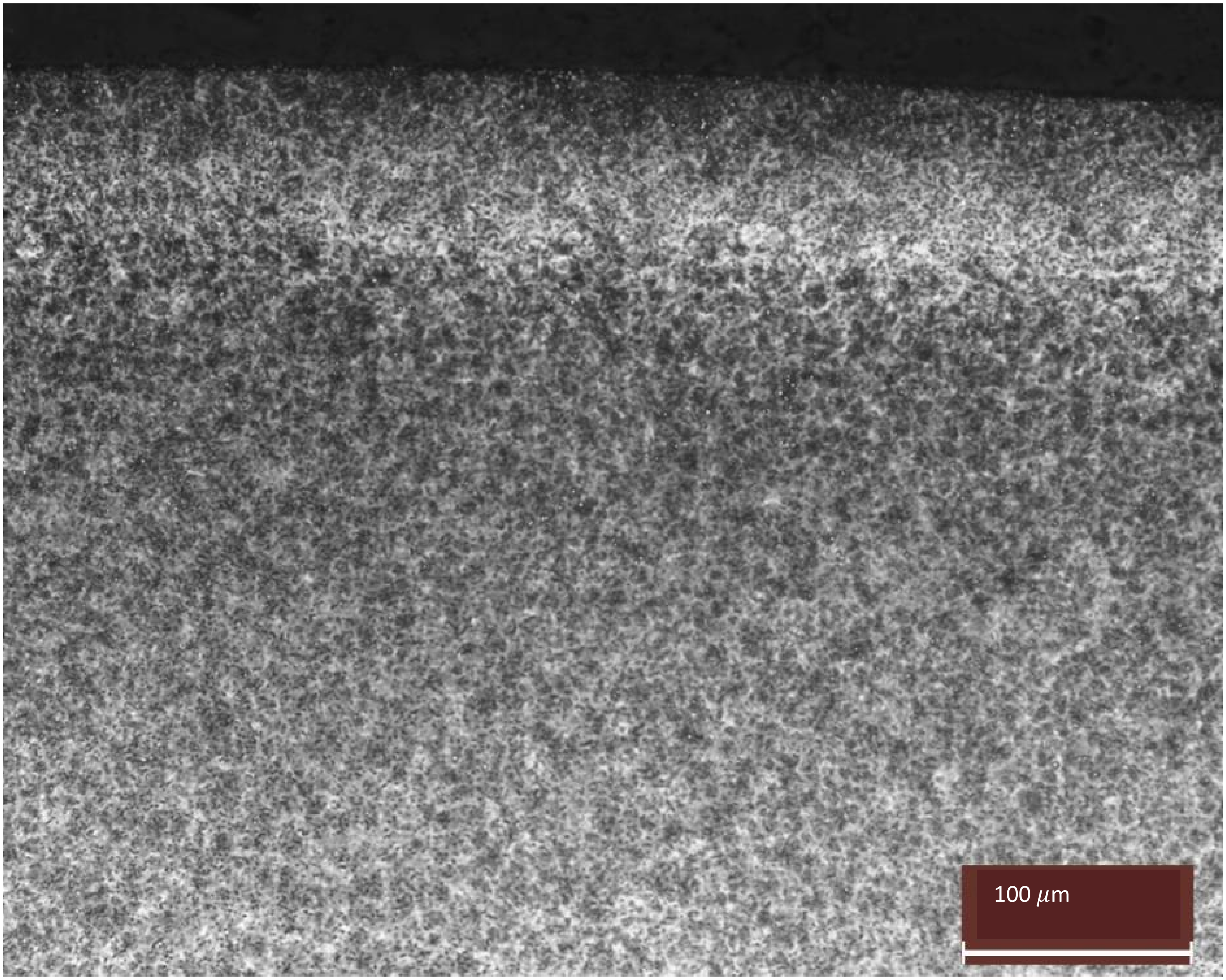

Figure 3.4 Dark etching area formation in 100cr6 steel

The adverse effect of dark etching area on rolling contact fatigue is not proven. However, DERs are associated with volumetric expansions of the material that culminates in excess amounts of residual stress which hinders crack propagation.

3.3 White etching bands

After DERs formation the next feature which will appear are white etching bands. And they occur inside dark etching area. They have characteristic directionality. There are two forms of bands. High-angle bands and low-angle bands. The first one is observed when the bearing has been exposed to a long service or the contact stress is very high. The low-angle bands form an angle of 20–35 degree [24]. The carbon content in these bands has been observed to be less than the parent matrix. It should also be taken into account that WEBs were reported normally to initiate after L_{10} life of the bearing.

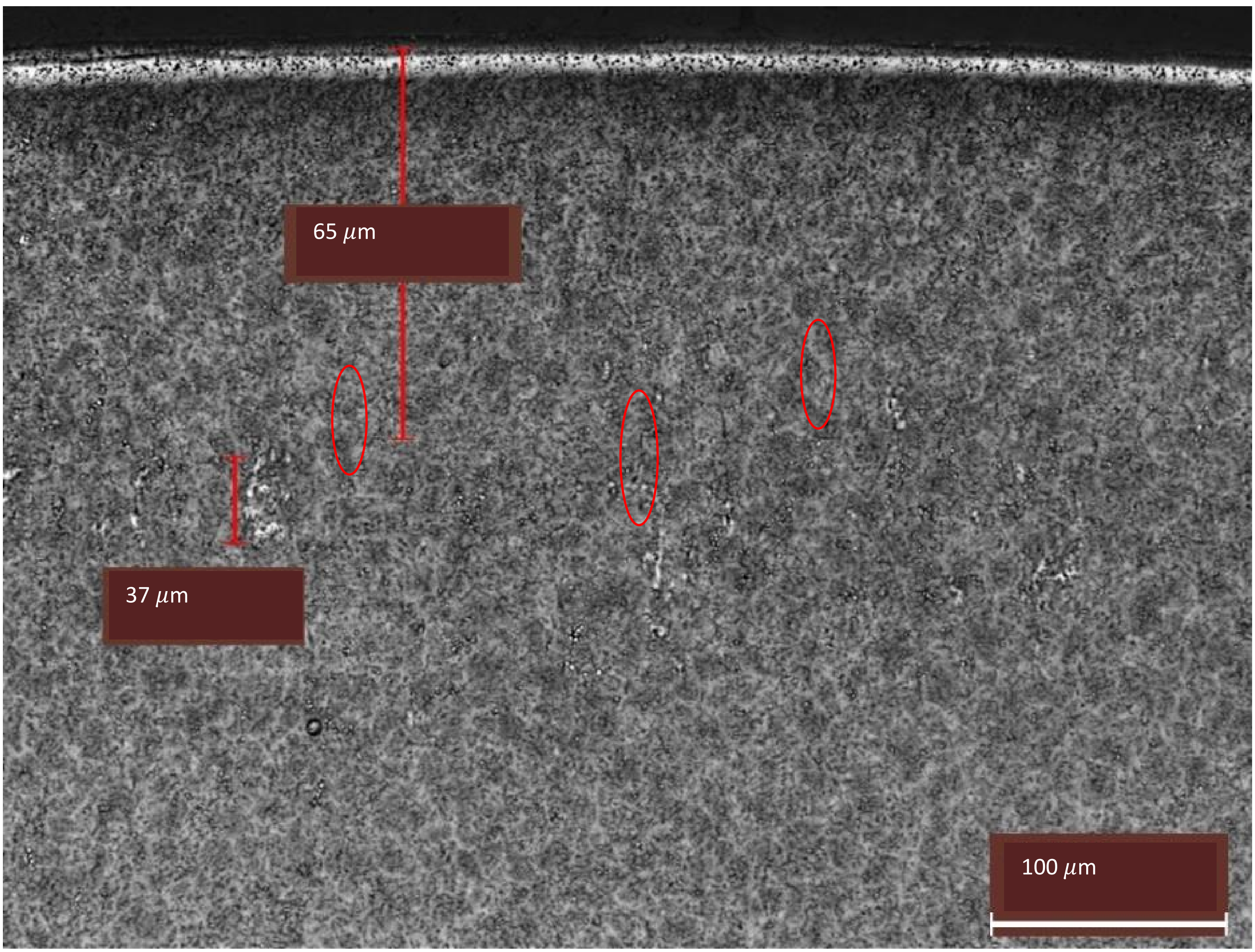

Figure 3.5- formation of high-angle bands in their early stage

Chapter 4

4. Production process

4.1 cycle of sphere production

The process develops in full at micron accuracies and takes place at starting with the use of a steel rod commonly used for bearings, 100cr6, regulated by ISO 683-17:2014. At this point operations are distinguished:

- Heading process
- Soft grinding
- Heat treatment
- Peening
- Surface finishing
- Quality control

4.2 Heading

The raw material from which the balls are made is a 100cr6 steel and it comes in forms of wire rods. According to the sphere type, the diameter of the wire rod varies.

Figure 4.1-steel wire rods

The wire rod, therefore, is unrolled and inserted into the press where two steps take place before molding: First of all, the steel wire is slightly drawn to make it uniform the diameter of the blank and then cut to obtain the cylinder, the dimensions of which (height and diameter) are parametrized according to the sphere type. Then we move on to real molding phase, in which the just cut cylinder is positioned inside the molds. The material is deformed by the mold caps up to obtain a rounded shape.

4.3 soft grinding

The sphere appearance after the heading process can be observed in (figure 4.2). In its defined characteristics two poles (bases of the small cylinder that do not were rounded during molding) and an area of stock, the equator, due to the excess of material pressed along the mold division plan. The sphere printed is still very far from finished product, despite the process forming is fundamental for the purpose of output quality of the finished product. An excessive deviation of the cutting phase of the wire rod or excess stock in the equatorial zone may indicate a poor-quality molding stage.

The products leaving the molding are then passed where the filing process is happening.

Figure 4.2- ball after filling process

Then the stock of poles and equator is removed thanks to the pressure developed on a single sphere by the grinding wheel. The machine is composed essentially by a motorized loader into which the batch of balls from working, and two discs on which series of grooves are made. One of the two, the grinding wheel, is in rotation at a certain number of constant revolutions guaranteed by a motor reducer. During processing the spheres are forced to pass through the grooves of the plates and grinding wheel along a full turn. A hydraulic system guarantees a constant plate pressure and grinds on the sphere that are passing through the grooves. The filling processing is guaranteed by the motion between spheres and plates which eliminates part of the stock in each pass. After a passage between plate and grinding wheel. The balls are returned to the magazine. All this process uses a lubricating coolant which is mainly water-based, which is then filtered and put back into circulation through a closed-circuit system

Figure 4.3- fixed cast iron plate

Figure 4.4- rotating cast iron plate

4.4 Heat treatment

The heat treatment separates the hard grinding processes or molding and filing, where it is generates a spherical shape in the rough and where there is the elimination of a good part of the excess stock, from soft grinding in which the sphere is finished and the stock in excess is very low. The heat treatment takes place in large electric furnaces. The handling of the balls is guaranteed by a series of augers which the balls move inside. The heat treatment can be divided into two phases: one first austenitization phase, in which the spheres are heated up to about 840 ° C. Subsequently, the spheres are hardened, suddenly cooling them in an oil bath. Finally, to avoid over-stress of the materials, the spheres are tempered at 160 ° C. On leaving the oven, the spheres are sieved by means of a selection system a vibrating comb to prevent other spheres of different diameters from being left in the augers and accidentally getting into the wrong batch. To verify that the balls we have reached the optimum hardness, in addition to spot checks, the balls come subjected to a quality test, the jump test.

4.5 peening

This processing is useful to further increase the surface hardness of the balls and produce a subsurface residual stress that can be beneficial if it is compressive and is in subsurface of the ball. The batch of spheres is introduced into a machine, which induces with its cyclic operation a sequence of repeated impacts between the spheres that become harder on the surface with increased compressive residual stress.

4.6 Surface finishing

Before the final phase, the spheres undergo a process substantially identical to the filings but with a less aggressive cut-rate. For this reason, the plate and grinding wheel are made of two different materials (cast Iron and Bakelite) in order to eliminate any stock in excess. Then the spheres are polished by grinding wheels and Bakelite plates. Here the spheres come mirror polished and slightly reworked with low cut-rates in the order of μm / h

4.7 Quality control

During quality control, each sphere passes through an electronic controller, which by means of an optical laser evaluates the surface and any defects, not otherwise detectable. An inductive probe generates a magnetic field inside the sphere and evaluates any lack of material. Therefore, if the sphere passes both checks, it can move on to the packaging otherwise it is rejected waiting for a second check.

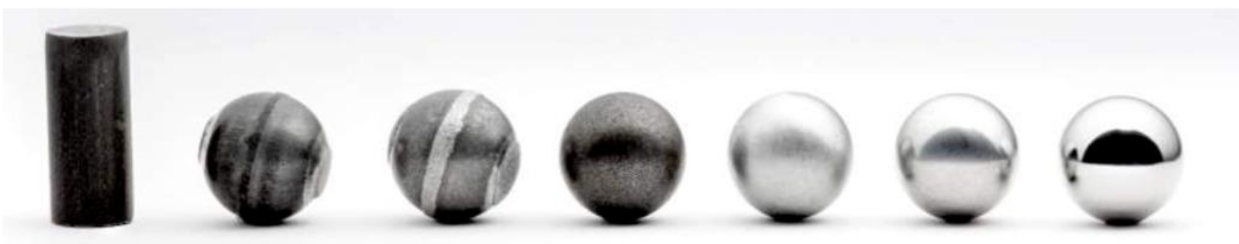

Figure 4.5-spheres in different parts of process

Chapter 5

5.Experimental methods

Experimental tests were made in order to get real data in order to estimate and observe the initiation of the cracks. Tests were conducted on finished product (Balls, d=11.112 mm), and raw material in order to obtain data of material in RCF. Rolling contact fatigue benches are used in this study to investigate failure due to micro-inclusions and imposed residual stresses. In order to characterize the fatigue behavior of raw material rotating bending fatigue tests on standard specimens were done. In order to understand the imposed residual stress and the changes in retained austenite, Xray diffraction tests were performed. After failure analysis was made when the fracture happened in either the specimen or the ball. And finally, a threshold parameter has been defined to estimate the fatigue life counting the combined effect of presence of inclusion and time varying residual stresses during operation.

5.1 Rotating bending fatigue tests

The starting material was a high carbon content 100Cr6 steel wire cut in samples of 150 *mm* length. Then in order to get the same properties of the produced balls, samples were heated above austenitization temperature at 850° *C* followed by quenching. Then the standard specimen was obtained according to ISO 1143 standard specification.

Figure 5.1 final specimen

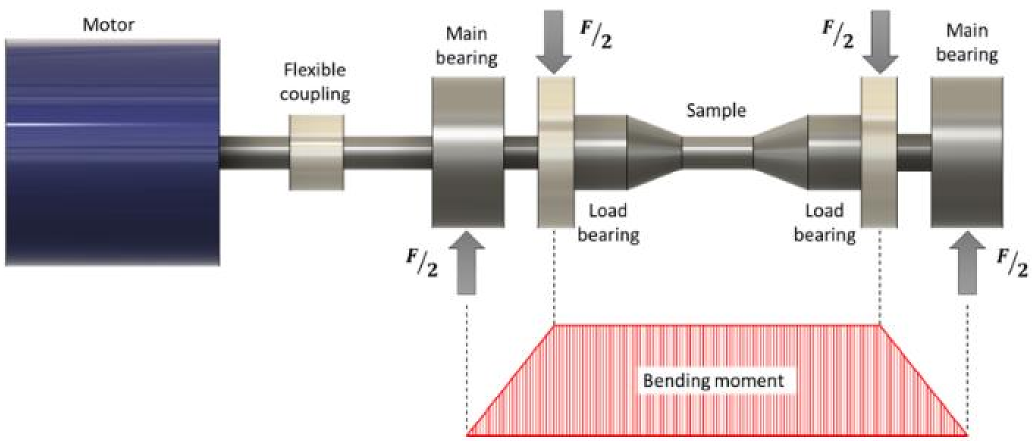

Figure 5.2-schematic representation of a four-point rotating bending machine

In order to satisfy the standard requirements Roughness of the specimen in 5 different locations (tangs, junctions, minimum cross section) is measured after polishing to know if they are in standard limits. The specimen should be free of any surface defects in order to make sure fracture was not caused by anything other than inclusion effect.

5.1.1 Staircase method

The staircase method is used to estimate the fatigue limit stress of the steel. The first specimen is subjected to a stress supposed to be the expected average fatigue strength. If the specimen survives the life target which is 5 million cycles, the test is stopped, and the next specimen is subjected to a stress that is one increment above the previous sample. When a specimen fails before reaching 5 million cycles, the obtained number of cycles is noted, and the next specimen is subjected to a stress that is one increment below the previous. The increment $\Delta\sigma$ is fixed before starting the test campaign. the next campaign the load increment is increased or decreased by $\Delta\sigma$ according to failure or survival of campaign the applied load is controlled by a PC software, as the rotational speed.

5.2 Test rigs for ball bearings

The fatigue test process for the balls is designed in a way to test balls without damaging the other parts of the bearing, like the inner ring, outer ring and cage. In order to ensure the reliability of different tests and so to have the same test conditions, a process protocol that is established since many years, was adopted. The same test states and settings are requisite to differentiate the fatigue life of different balls. Because of the high contact pressure between the balls and the raceways, it could be possible to have a damaging of inner and outer rings that consequently generates balls damaging which invalidate the test. Some of the test rigs main part are:

1. Electric motor
2. Shaft
3. Hydraulic piston
4. Pneumatic piston
5. Vent
6. Accelerometer
7. Thermocouple
8. Protective shell
9. Flange
10. Command system

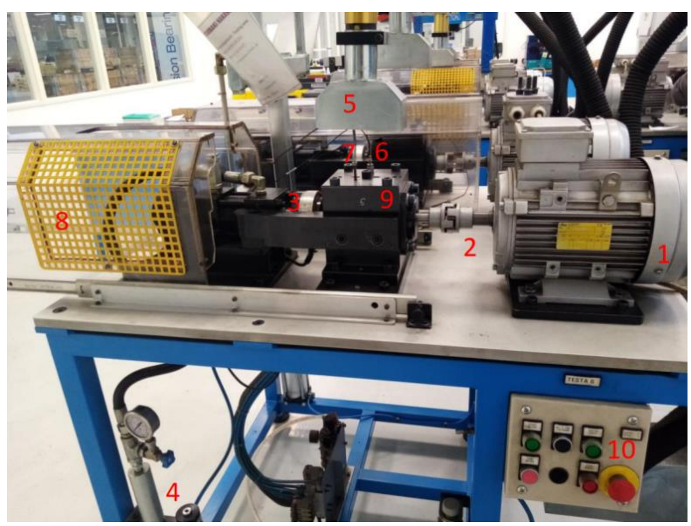

Figure 5.3Test rig

On each of the test rigs two type of Hub application bearings can be mounted. angular contact ball bearings of ø11.112 mm and ø10.5 mm can be mounted on test rigs but the balls that are target in this study are ø11.112 mm balls.

The motion is transferred with the help of electric motors connected to the shaft. Bearing is mounted on the shaft by interference fit and fixed to the structure by flange. The bearings are imposed to axial load by a hydraulic piston. The protective shell ensures the operator to work safely. A ventilation system is located above each test rig in order to prevent overheating. In order to ensure the testing condition stays within the limits and does not defer from nominal condition some important parameters such as temperature, acceleration, and load level is measured using thermocouple, accelerometer and load cell sensors and the data is reported on the computer connected to test rigs every minute.

- A high level of load may produce high pressure on balls that leads to premature failure
- A high temperature can arise due to excessive or limited lubricant, or a marked Sphericity of the balls and so excessive contact pressure
- A high level of vibrations may suggest a marked Sphericity of the balls or a failure of one of the bearing components.

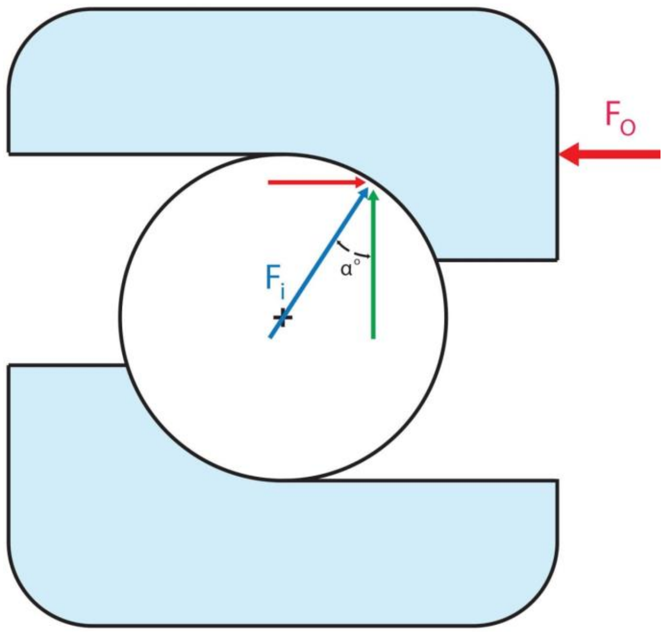

Figure 5.4 forces in angular contact

$$F_n = \frac{F_O}{z \sin \alpha} = 10467\text{N}$$

- Z = Balls tested: 7
- F_o = Axial force applied on bearing: 34400 N
- F_n = Force that acts on the normal direction of the contact =10467N
- α = Angular contact: 28°

In order to increase the contact pressure between the ring and balls only 7 balls in one row was used instead of 14 balls since the load is applied purely in axial direction (this is the load applied by the hydraulic piston to the outer raceway). The grease used is the Shell Gadus S3 V220. since any contamination of the lubricant can lead to a reduction in the bearing fatigue life assembling the components should be done precise and clean.[20]

The test conditions are summarized below:

• Ball material: 100Cr6

- Ball diameter: $\o 11.112\ mm$
- Ball number in each no-test bearing: 15
- Ball number in each test bearing: 7
- Applied Load: 34400 N
- Grease for tested balls: Shell Gadus S3 V220
- Load limit: 37500 N
- Vibration limit: 15 $\frac{mm}{s^2}$
- Temperature limit: $145^{\circ}C$
- Life target: 200h
- Shaft speed: 690 Rpm
- Releasing load interval: 25s every 300s
- Data acquisition period: 60s
- inner raceway radius in radial direction: 6.322 mm
- inner raceway radius in circumferential direction: 22.25 mm

The test can start when the two bearings are mounted on the shaft and the bench is correctly assembled. During the firsts 10 minutes, the load is only the 30% of the nominal one to obtain a homogeneous distribution of the lubricant and the optimal centering of the shaft. After this short time, the load is raised until the nominal one. Every 5 minutes the load is released for 25 seconds to allow the spinning of the balls. Each 20 hours the rigs are stopped so as to change the rings, the lubricant, the cages, and the balls of the no-tested bearing. In this way, the element of the bearing that will fail earlier will be the ball in most cases.

5.2.1 reason for premature stops in test rigs

1. **High temperature**

If the temperature overcomes $145^\circ C$, the machine stops. This temperature was chosen because $150^\circ C$ is the tempering temperature of the steel, over this limit there is the possibility of microstructural changes (hardness reduction) of the rolling elements and then a reduction of fatigue life.

2. **Vibrations**

When the vibrations level is higher than $15 \frac{mm}{s^2}$, the machine stops. That level was chosen according to the testing developed experience: if a lower level is set, the machine would stop for external vibrations and if a higher level is set, a ball could be broken but the machine would not stop, ruining the test.

3. **Load**

In order to prevent the overload, the test is stopped if the load limit is exceeded. At every stop of the bench, it must be disassembled and cleaned. The components must be inspected completely, and different situations can arise:

• Stops **before** 20 hours:

The test bearing (BAHB-311396B Hub bearing)has to be inverted or changed if both sides have been already used, while the rings of the support bearing can be maintained if they are in good status. The φ 11.112 mm balls must be changed.

• **Programmed** stops at 20 hours:

Both the test bearing and the support bearing must be inverted or changed, as the φ 11.112 mm balls. After this operation, everything is lubricated and assembled. This accurate maintenance ensures that the balls break first. Moreover, at each stop, the roundness and weight of the balls is measured to know the damage evolution.

The test is considered finished in two cases:

• Failure of the tested balls.

• Excessive vibrations or temperature due to a ovality of the balls.

5.3 inspections on tested balls

The analysis that are performed on failed balls are as below:

1. The failed balls are inspected under stereomicroscope to investigate the nucleation point of the crack. In order to do so a few photos at different angles and magnification is taken.
2. In order to know the chemical composition of the inclusion scanning electron microscope is being used.
3. The residual stress state of the ball at different depth was measured using Xray diffractometer.
4. Retained austenite content of the balls are measured in order to know its changes for different testing condition.
5. The depth of failure for each failed ball was measured using a gauge-meter(see figure 5.7).

Figure 5.5-stereomicroscope *Figure 5.6-scanning electron microscope*

Figure 5.7gauge-meter

5.4 Elastic-plastic materials: shakedown

In this part we are investigating the behavior in rolling contact of bearing steels which are perfectly elastic up to a yield stress point: R_e in simple tension or compression, “k” in simple shear. after yielding they deform in a perfectly plastic manner. Yield first takes place at a point below the surface when the maximum contact pressure $P_{max} = c \times R_e$, where c is a constant (= 1.7) whose value depends on the geometry of the contact and the yield condition. Maximum contact stress at the center of contact surface, at yield onset, is obtained as follows:

$$\sigma_{eq} = \sigma_z - \sigma_y = 0.63P_{max} = R_e$$

$$P_{max} = \frac{R_e}{0.63} \cong 1.7R_e$$

Yield onset R_e for bearing steels is around 1800÷2100 Mpa[25]. So, if we consider R_e=2100 Mpa maximum pressure will produce yield when $P_{max} \cong 3570\ Mpa$

at the onset of yielding, the magnitude of the shear yield stress “k” in pure shear is (√3) times less than R_e which gives us:

$$k = \frac{R_e}{\sqrt{3}} \cong 1212\ Mpa$$

In rolling contact the bearing have to resist many repeated passes of the load. If the elastic limit is surpassed in the first pass some plastic deformation will occur and thereby introduce residual stresses. In the second passage of the load steel is subjected to the combined action of the contact stresses and the residual stresses introduced in the previous pass. Such residual stresses are protective in the sense that they make yielding less likely on the second pass. If the residual stresses build up to significant values, it is possible that after a few passes subsequent passes of the load result in entirely elastic deformation. This is the process of shakedown under repeated cyclic load, whereby initial plastic deformation introduces residual stresses which make the steady cyclic state purely elastic[26]. The shakedown limit for the given cyclic loading, is the highest stress which can be applied and will not cause plastic deformation.

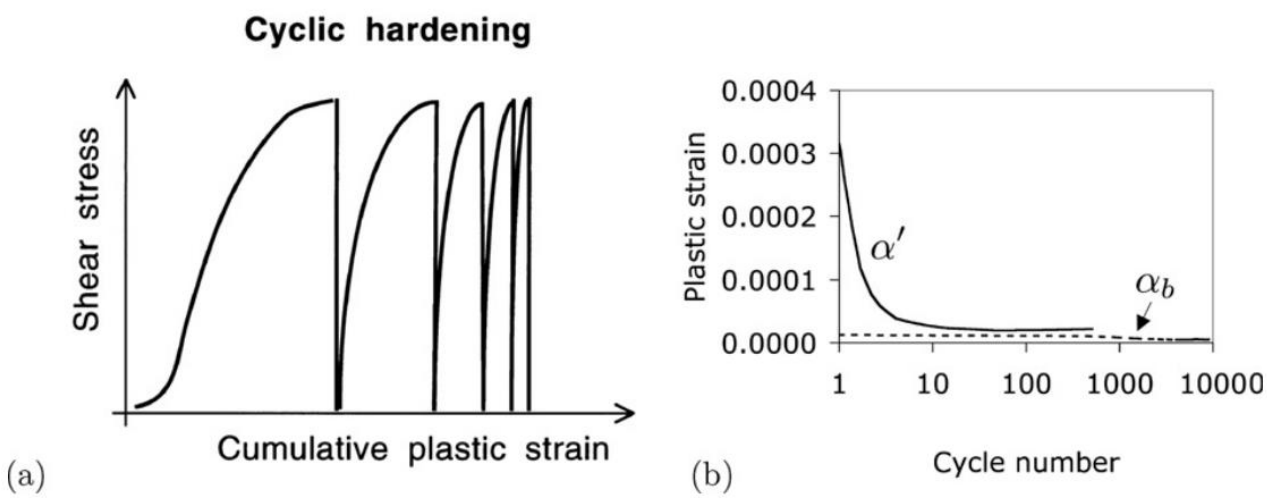

Figure 5.8 (a) Schematic illustration of constant stress–amplitude fatigue test leading to shakedown, i.e., a point where the plastic strain ceases to increase. (b) Plastic strain as a function of the number of cycles, for 52100 steel in its martensitic $(\alpha)'$ and bainitic (α_b) conditions; data from [1]

Melan's theorem states if any time-independent distribution of residual stresses can be found which, together with the elastic stresses due to the load, forms a system of stresses within the elastic limit, then the shakedown will occur in material. On the other hand, if such distribution of residual stresses cannot be found, then the shakedown will not occur and plastic deformation will happen at every passage of the load. Now the possible distribution of residual stresses remaining in the half space after cyclic loading will be considered. By assuming plane deformation $(\tau_{xy})_r$ and $(\tau_{yz})_r$ (suffix r denotes residual stress) will be eliminated. So remaining components are independent of y. The residual stresses are independent of "x" If plastic deformation is assumed to be steady and continuous. the surface of the half-space will remain flat. Finally, for having equilibrium with a traction free surface $(\sigma_z)_r$ and $(\tau_{zx})_r$ cannot exist in the residual stresses.

Therefore, the remaining possibility for system of residual stresses reduces to:

$(\sigma_x)_r = f_{1(z)}$, $(\sigma_y)_r = f_{2(z)}$ and $(\sigma_z)_r$=$(\tau_{xy})_r$=$(\tau_{yz})_r$=$(\tau_{zx})_r$= 0

After combination of contact and residual stresses, principal stresses are obtained as:

$$\sigma_1 = \frac{1}{2}(\sigma_x + (\sigma_x)_r + \sigma_z) + \frac{1}{2}[\{\sigma_x + (\sigma_x)_r - \sigma_z\}^2 + 4\tau_{zx}^2]^{\frac{1}{2}}$$

$$\sigma_2 = \frac{1}{2}(\sigma_x + (\sigma_x)_r + \sigma_z) - \frac{1}{2}[\{\sigma_x + (\sigma_x)_r - \sigma_z\}^2 + 4\tau_{zx}^2]^{\frac{1}{2}}$$

$$\sigma_3 = \nu\{\sigma_x + \sigma_z\} + (\sigma_y)_r$$

Following Melan's theorem, in order to avoid yield we can choose the residual stresses to have any value at any depth. Thus $(\sigma_y)_r$ can be chosen to make σ_3 the intermediate principal stress. Then to avoid yield, by the Tresca criterion,

$$\frac{1}{4}(\sigma_1 - \sigma_2)^2 \le k^2$$

where k is the yield stress in simple shear, i.e.

$$\frac{1}{4}\{\sigma_x + (\sigma_x)_r - \sigma_z\}^2 + \tau_{zx}^2 \le k^2$$

If τ_{zx} exceeds k, the equation cannot be satisfied and it can only be satisfied with τ_{zx}= k if we choose $(\sigma_x)_r = \sigma_z - \sigma_x$. Thus, the limiting condition for shakedown happens only if maximum value of τ_{zx} anywhere in the steel gets to k. The maximum value of τ_{zx} is at 0.25 P_{max} , So shakedown takes place whenever P_{max} ≤4.00 k. Also by using von Mises criterion same results are achieved. The ensuring residual stresses at a depth 0.50a in order to cause shakedown are:

$$(\sigma_x)_r = -0.131P_{max}\ ; \quad (\sigma_y)_r = -0.213P_{max}$$

By von Mises criterion the value of P_{max} for first yield is 3.1 k. So, the ratio of the shakedown limit load to the elastic limit load is:

$$\frac{P_s}{P_Y} = \frac{(p_{max})s^2}{(P_{max})R_e{}^2} = 1.66$$

Which says that the load must be increased by more than 66% above the first yield load to cause continuous plastic deformation in rolling contact. The

changes to the stresses at z = 0.5a by adding the residual stresses are shown by the broken lines in the figure below

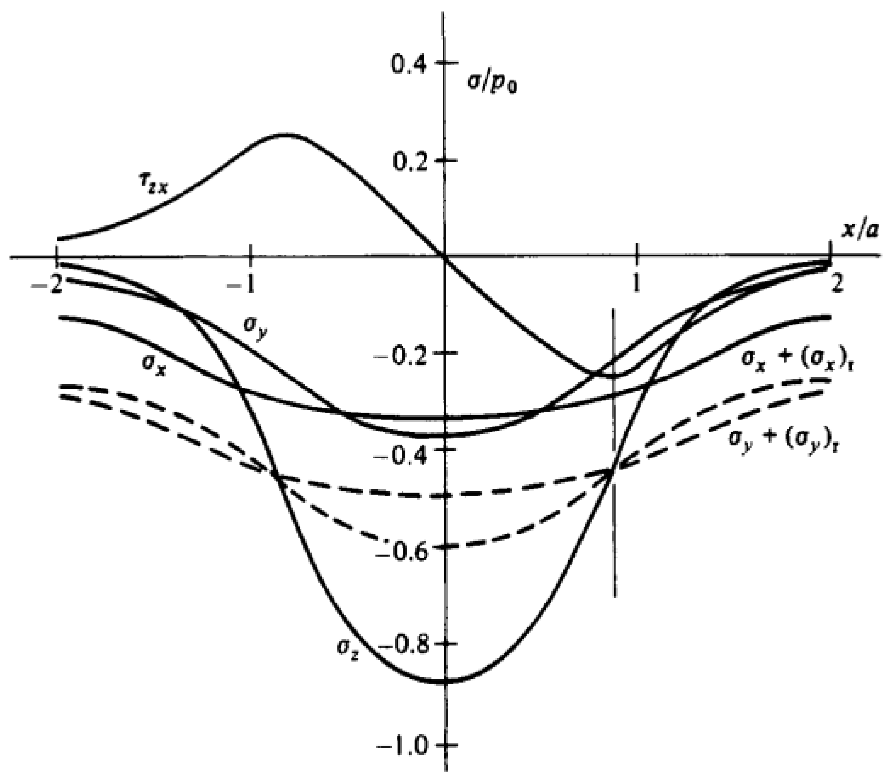

Figure 5.9 Solid line – elastic stresses at depth z = 0.5a. Broken line - with addition of $(\sigma_x)_r$ and $(\sigma_y)_r$ for shakedown.

The application of Melan's Theorem to three-dimensional rolling bodies is much more complicated since all components of residual stress can arise, and since a flat surface does not remain flat after deformation. If we consider the plane of symmetry ($y = 0$) of a ball rolling on an elastic-plastic half-space, by symmetry $\left(\tau_{xy}\right)_r = \left(\tau_{yz}\right)_r = 0$, but a residual shear stress$(\tau_{zx})_r$ can exist. However, τ_{zx} due to a purely normal contact load has equal and opposite maxima on either side of $x = 0$. Thus, yield cannot be inhibited by the addition of a unidirectional residual stress. It follows, therefore, that the shakedown limit is again governed by the maximum value of $(\tau_{zx})_r$.t If the reduction in contact pressure due to the formation of a shallow plastic groove is neglected then $(\tau_{zx})_r$ = 0.21P_{max},, whereupon for shakedown:

$$P_{max} \leq 4.7k \cong 5700\ Mpa$$

By von Mises, the value of P_{max} for first yield is 2.8k, hence

$$\frac{P_s}{P_Y} = \left(\frac{4.7}{2.8}\right)^3 = 4.7$$

which is a much larger factor than in the two-dimensional case.

In this study we obtain the maximum Hertzian pressure at contact for the load that we apply in test rigs and to compare the maximum contact pressure with the shakedown limit. Also, by calculating the maximum orthogonal shear stress location, a better understanding of most probable fracture location will be achieved.

Table 5.1 data obtained for the load applied to the test rigs

First radius body 1	r_{11}	5.5500	mm
Second radius body 1	r_{12}	5.5500	mm
First radius body 2	r_{21}	-6.2300	mm
Second radius body 2	r_{22}	22.2400	mm
Angle between planes for radii	α	0.00	°
Youngs modulus body 1	E_1	210000.00	MPa
Poisson number body 1	υ_1	0.35	
Youngs modulus body 2	E_2	210000.00	MPa
Poisson number body 2	υ_2	0.35	
Normal force	Fn	10050.00	N
Hertzian stress	pH	5746.84	MPa
Major half axis of contact ellipse	a	2.0225	mm
Minor half axis of contact ellipse	b	0.4128	mm
Approach of both bodies	δ	0.0594	mm
Maximal shear stress body 1	τMax_1	1814.75	MPa
Depth for max. shear stress body 1	$z(\tau Max_1)$	0.3075	mm
Maximal octahedral shear stress body 1	$\tau OctMax_1$	1538.22	MPa
Maximal shear stress body 2	τMax_2	1814.75	MPa
Depth for max. shear stress body 2	$z(\tau Max_2)$	0.3075	mm
Maximal octahedral shear stress body 2	$\tau OctMax_2$	1538.22	MPa
Maximal orthogonal shear stress	τyz	1422.33	MPa
Depth for max. orthogonal shear stress	$z(\tau yz)$	0.2005	mm

As we can see the Hertzian contact pressure is around the shakedown limit, but we have to take into account that the work hardening which results from the microplasticity elevates the yield strength and also the plasticity is probable to enlarge area of contact and therefore a reduction in the contact pressure may occur which in turn can increase the shakedown limit.

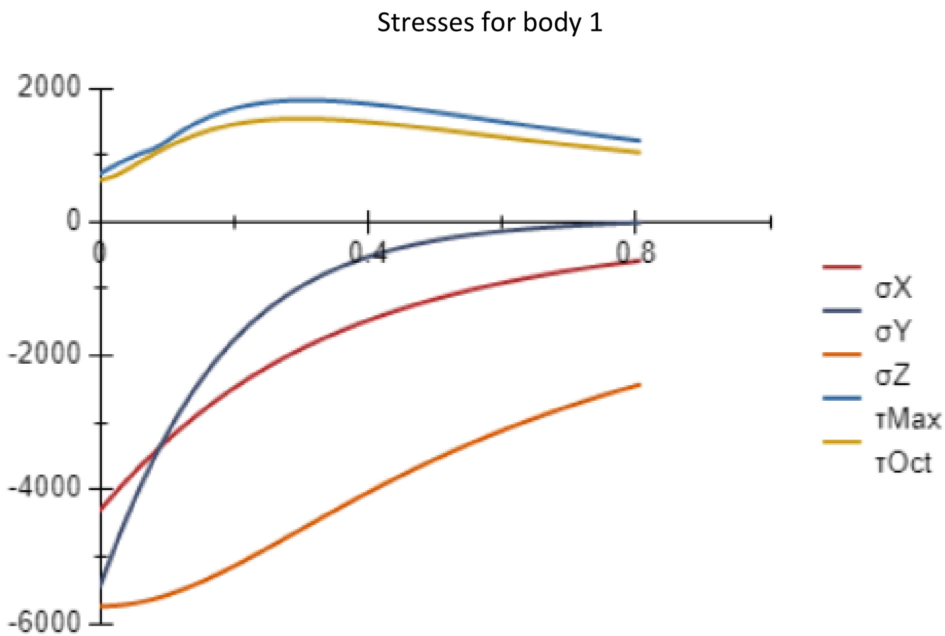

Figure 5.9 Diagram of stresses after applying load

5.5 Residual stress measurement

X-ray methods for measuring residual stresses in crystalline materials have been tested and are in use throughout the world. For small parts, or samples whose shape is not too complex or bulky, ordinary commercial diffractometers are quite adequate and offer the added advantage that such instruments can also be used for a variety of other measurements such as retained austenite, or preferred orientation. With the X-ray instrument that is used for this study exists a computer control and will permit software development for stress measurements.

Figure 5.10-X-ray diffractometer

For measuring the residual stresses in depth, a layer removal technique was used.

Residual stress measurements were made on the surface of ball after successively removed layers. Electropolishing was used in order to remove the material at each depth. ball is immersed in a temperature-controlled bath of electrolyte and serves as the anode;

it is connected to the positive terminal of a DC power supply; the negative terminal being attached to the cathode. current passes from the anode, where metal on the surface is oxidized and dissolved in the electrolyte, to the cathode.

5.4.1 Measurement Principle

When an atom is irradiated with X-rays, the electronic cloud around atom moves, like what happens to any electromagnetic wave. Variation of these charges causes radiated waves with the same frequency, unfocused a bit due to a variety of causes; this phenomenon is known as Rayleigh scattering (or elastic scattering).

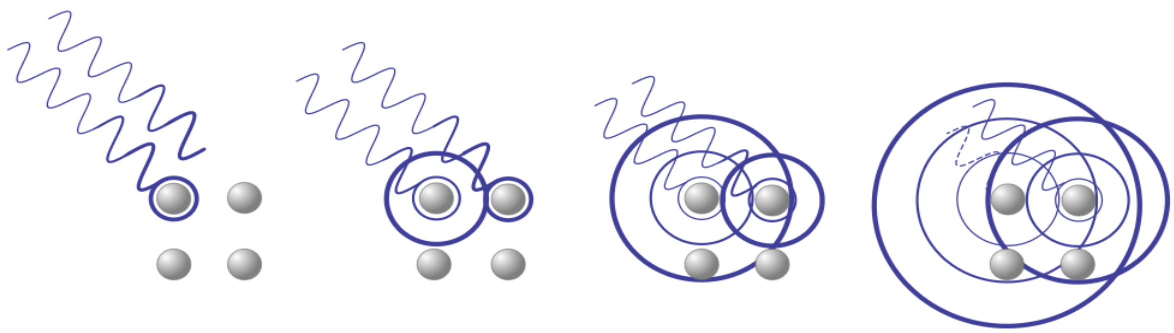

Figure 5.11-an atom irradiated with X-ray

Diffraction methods of residual stress determination basically measure the angles at which the maximum diffracted intensity occur when a crystalline sample is irradiated with x-rays from these angles one then obtains the spacing of the diffracting lattice planes by using Bragg's law. If the material is under load, these values will be different than the unstressed plane spacing, and the difference will be proportional to the stress acting on the planes.[27]

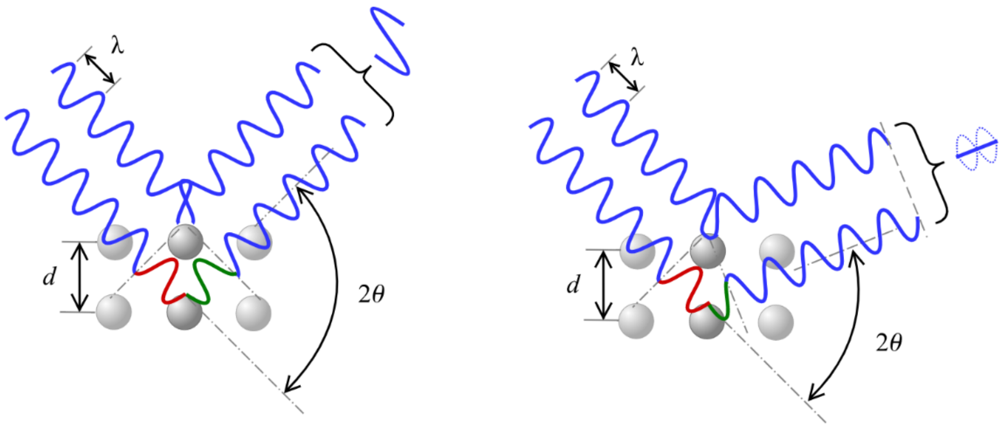

Figure 5.12 According to the 2ϑ deviation, the phase shift causes constructive (left figure) or destructive (right figure) interferences

When radiation occurs with a wavelength which is comparable to atomic spacing in a way which constructive interferences occur Bragg diffraction happens. The waves scatter from lattice planes which are separated from each other by interplanar distance d. the constructive interference happens when the different path length of two waves are integer multiple of wavelength. Constructive interference which is diffraction will happen when:

$$2\,d\sin\theta = n\lambda$$

The path difference is 2dsinθ, where θ is the reflection angle (see figure 5.9) n is a positive integer number and λ is the wavelength of the irradiated wave. If we measure the intensity of scattered waves as a function of various scattering angle a diffraction pattern is resulted. Very strong intensities known as Bragg peaks are obtained in the diffraction pattern at the points where the scattering angles satisfy Bragg condition. The constructive or destructive interference intensifies because of the cumulative sequel of reflection in consecutive crystallographic planes (h,k,l) of the crystalline lattice.

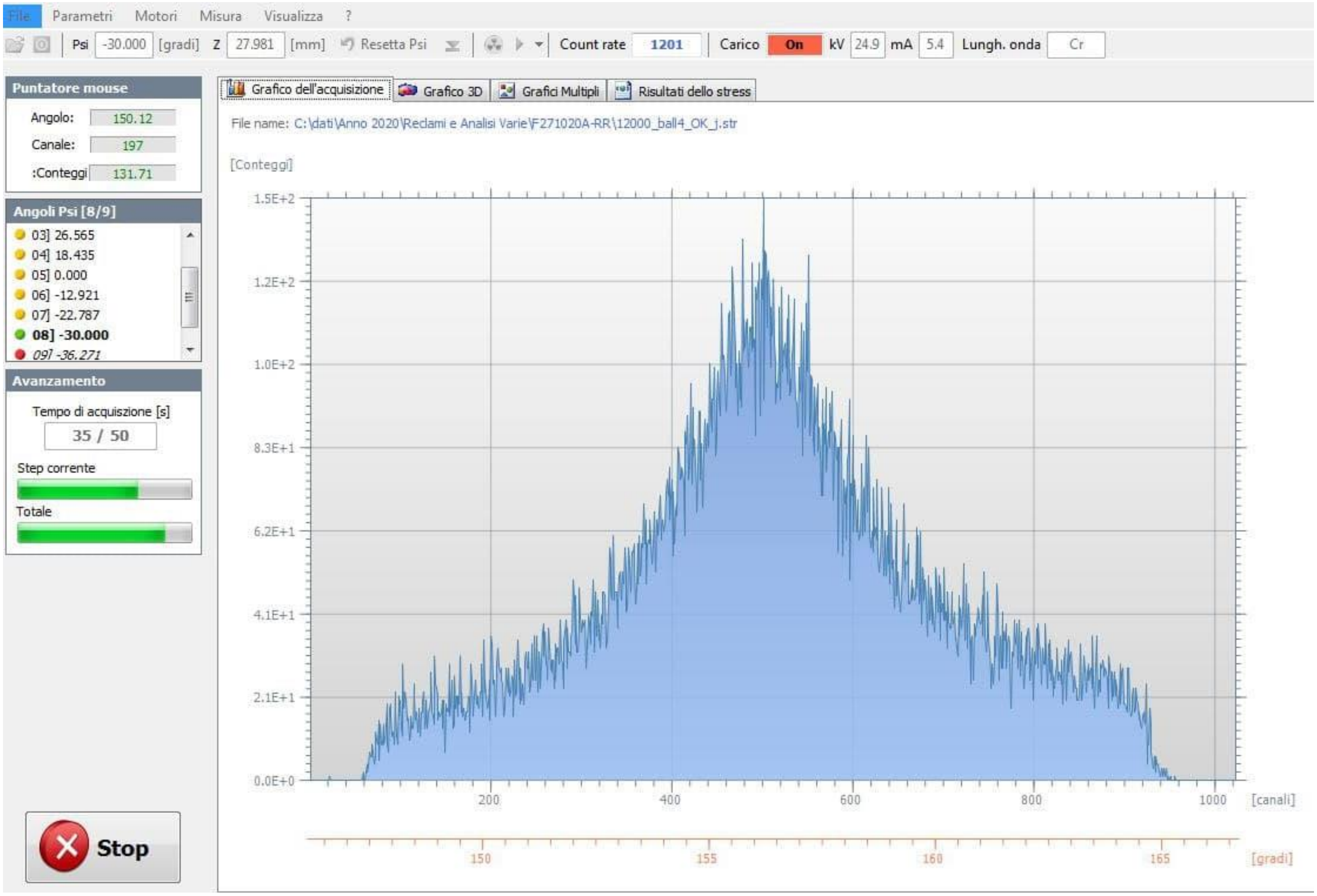

Figure 5.13- Variation of intensity with diffraction angle predicted by the Bragg law. Line broadening caused by deviation from the theory. (measurement software in Pinerolo)

5.4.2 Analysis of Regular "d" vs. $\sin^2 \Psi$ Data

The coordinate systems used in the following are shown in Fig. 5.11. the axes S_i define the surface of the ball. The laboratory system L_i is defined such that L_3 is in the direction of the normal to the family of planes (h,k,l) whose spacing is measured by x-rays. Once the lattice spacing, $d_{\phi\Psi}$ is obtained from the position of the diffraction peak for a given reflection (h,k,l,) the strain along L_3 may be obtained from the formula

$$(\varepsilon'_{33})_{\phi\Psi} = \frac{d_{\phi\Psi} - d_0}{d_0} = \varepsilon_{11} \cos^2 \phi \sin^2 \Psi + \varepsilon_{12} \sin 2\phi \sin^2 \Psi + \varepsilon_{22} \sin^2 \phi \sin^2 \Psi$$

$+\varepsilon_{33}\cos^2\Psi + \varepsilon_{13}\cos\phi\sin 2\Psi + \varepsilon_{23}\sin\phi\sin 2\Psi$

Where d_0 is the unstressed lattice spacing. This strain can be expressed in terms of the strains ε_{ij} on the ball coordinate system by the tensor transformation

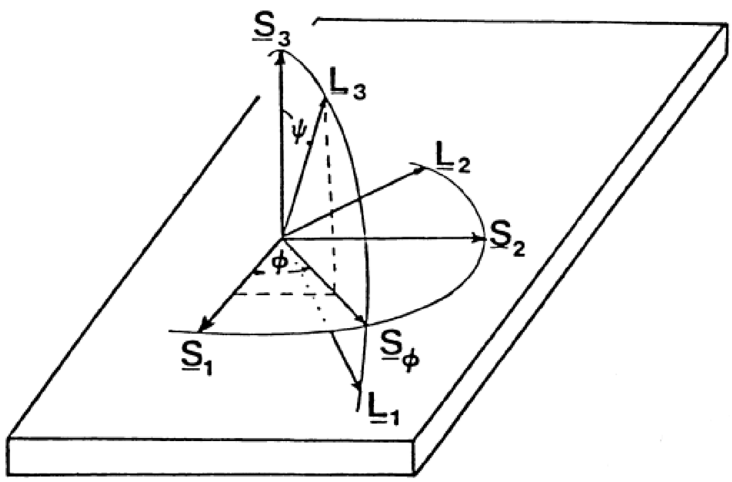

Figure 5.14-definition of laboratory coordinate system and the angles

In polycrystalline materials, where it is possible to obtain a diffracted beam, and thus a "d" spacing at all Ψ-tilts, three basic types of "$d_{\phi\Psi}$" vs. $\sin^2\Psi$ behavior are observed. For this study only one of these behaviors is concerned which is when "d ϕΨ " vs. sin2Ψ is linear. [27]A simple approach can be used for linear "$d_{\phi\Psi}$" vs. sin2Ψ plots. In this case, the strain tensor in the Si coordinate system is of the form:

$$\varepsilon_{ij} = \begin{vmatrix} \varepsilon_{11} & \varepsilon_{12} & 0 \\ 0 & \varepsilon_{22} & 0 \\ 0 & 0 & \varepsilon_{33} \end{vmatrix}$$

Once the strains are obtained, the stresses in the S_i coordinate is calculated by the general Hooke's law.

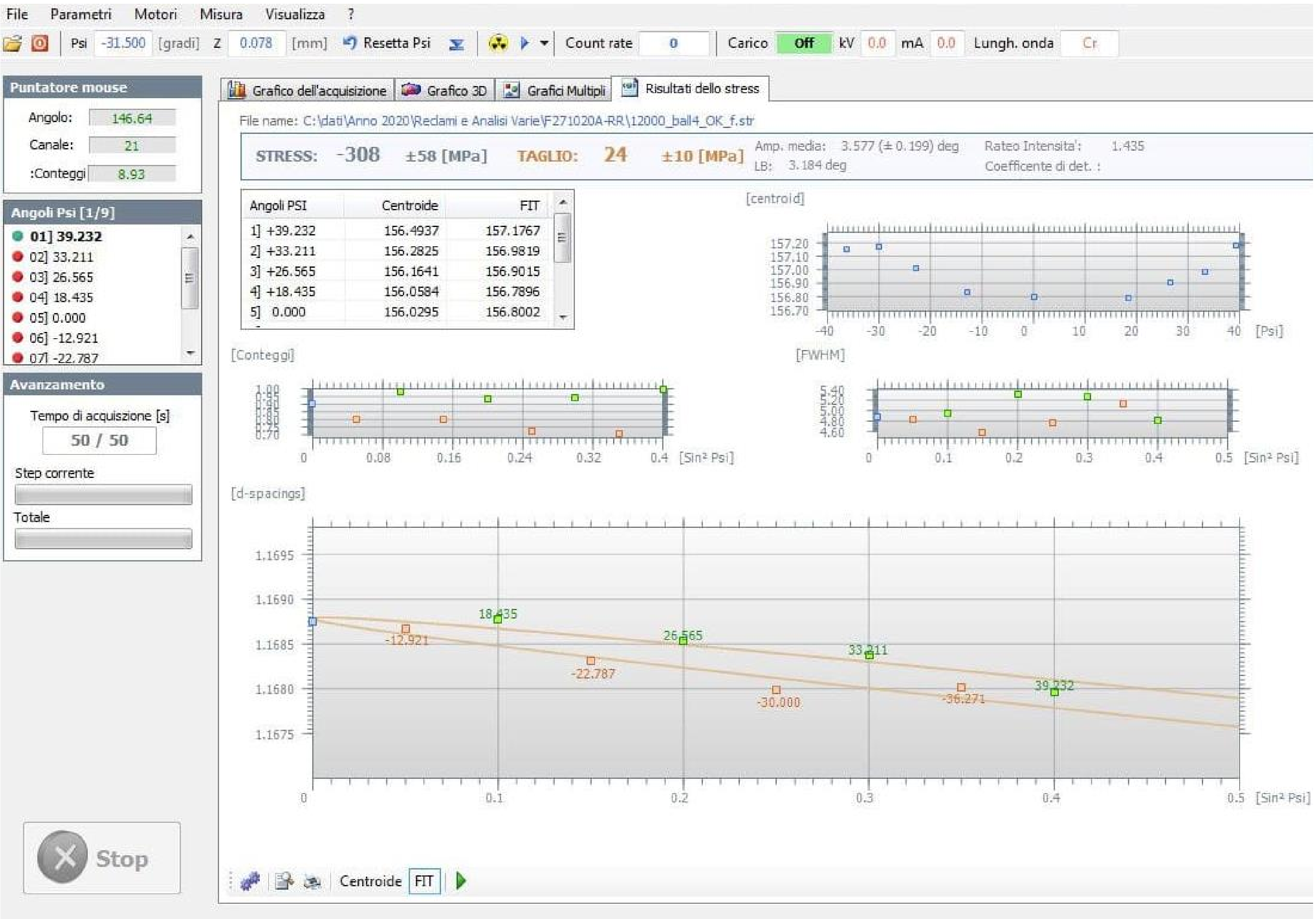

Figure 5.15-linear "d φΨ " vs. sin2Ψ behavior observed by residual stress software

Chapter 6

6.Results

The data corresponding to 32 broken balls which were tested on test rigs was gathered. The first step was to measure all the depths of the fractures by the gauge meter. Then an average value was calculated. The data are reported in table (6.1). (numbers are in μm)

	1	2	3	4	5	6	7	8	9	10	11	12	13
Test 1	-502	-348	-453	-177	-162	-300	survived	-570					-358.8571429
Test 2	-453	-562	-600	-284	-436	-326	-450						-444.4285714
Test 3	-386	-538	survived	-191	-626	-544	-347	-372	-573	-346	-162	survived	-408.5
Test 4	-320	-345	-662	-479	-320	-446	-292	-248					-389
												average=	-400.1964286

6.1-Microstructural alterations

When one of the seven balls assembled in the bearing fails, the test stops. In order to see the microstructural alterations happening from the other six balls which has no visible surface defects one was chosen. The balls then were cut and etched with nital-picral acid and then under optical microscope were observed. The microstructural alterations observed from the ball chosen from one of the six not failed balls is reported here in order

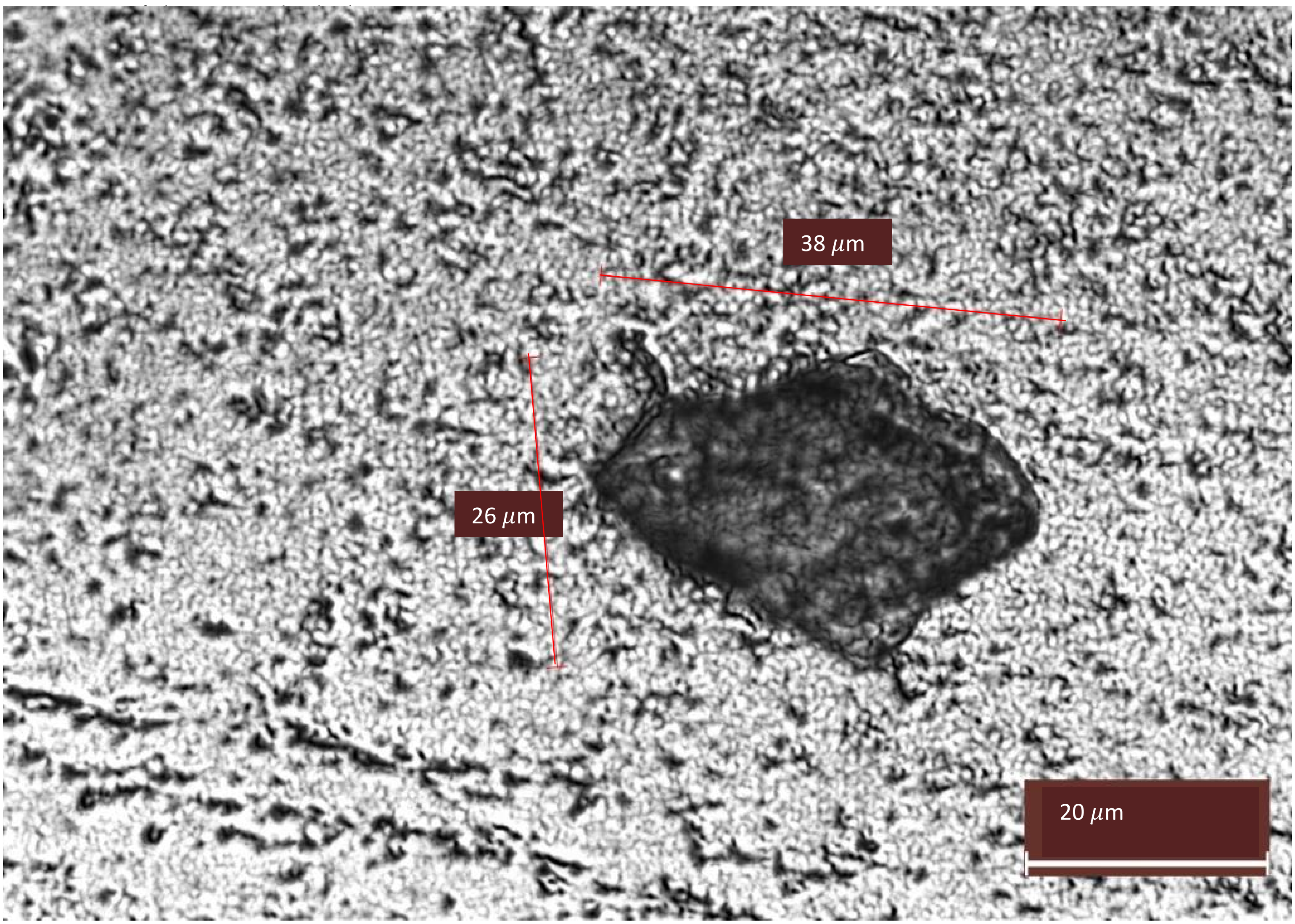

Figure 6.1-initiation of crack around an inclusion after 7.5h of test

In figure 6.1 we can see the initiation of crack which is happening diagonally at the two opposite ends of inclusion.

Figure 6.2- cracks observed after 10.7h of test around an inclusion

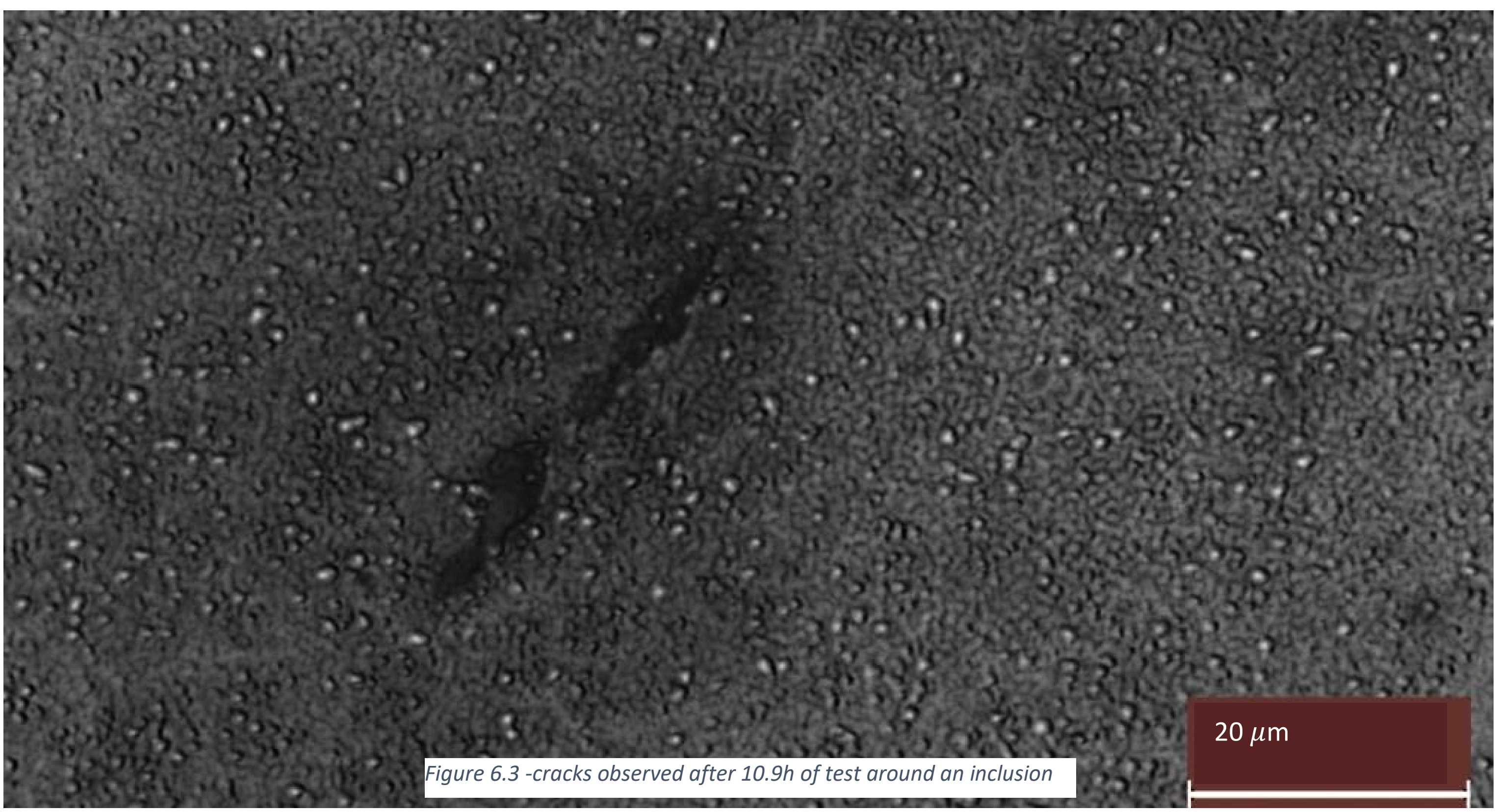

Figure 6.3 -cracks observed after 10.9h of test around an inclusion

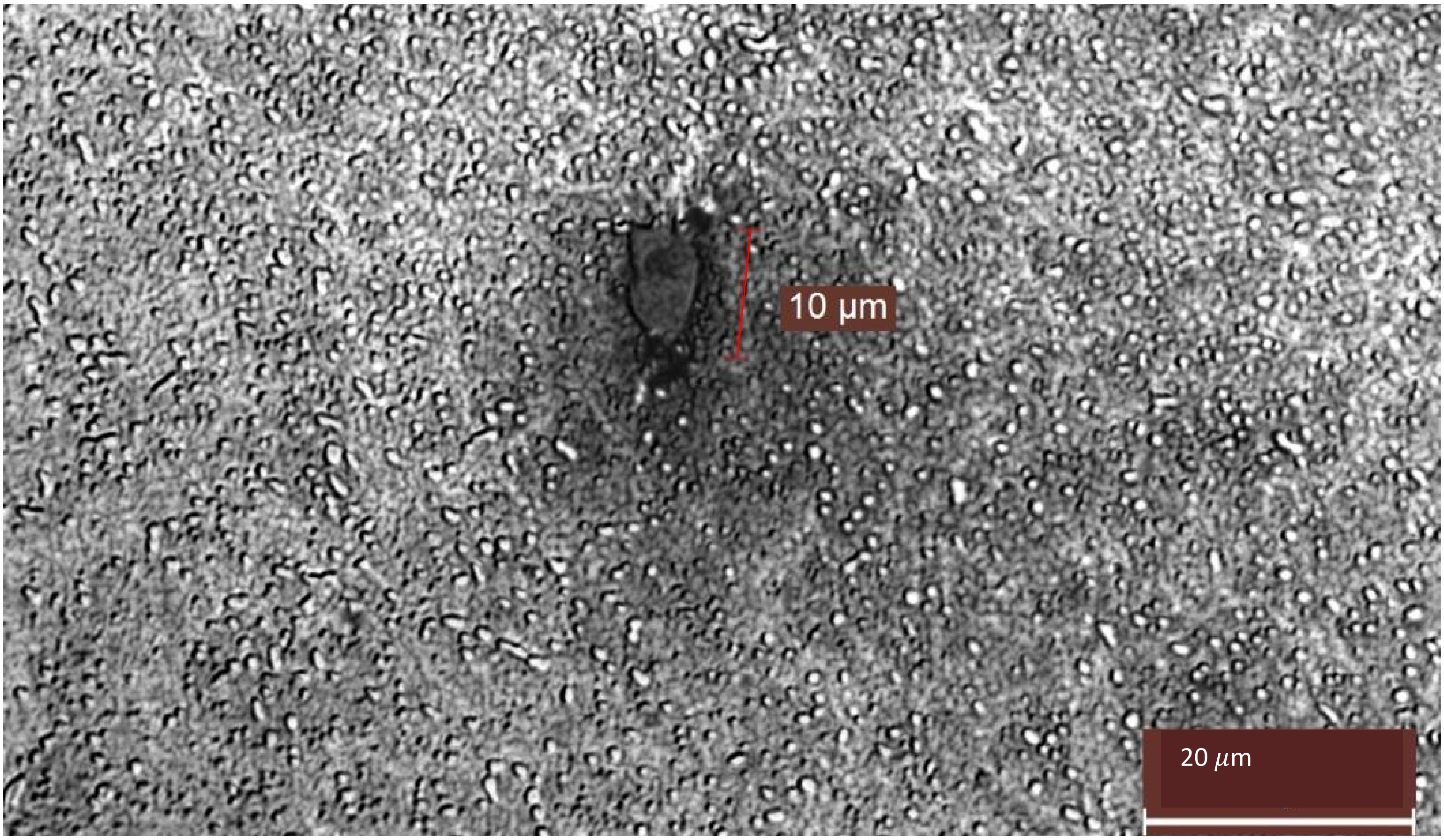

Figure 6.4-crack initiation around an inclusion after 14.7h of test. as we can see the inclusion is not well attached to the surrounding steel matrice.

the formation of butterflies can also happen only in one side of inclusion as we can see in figure 6.5.

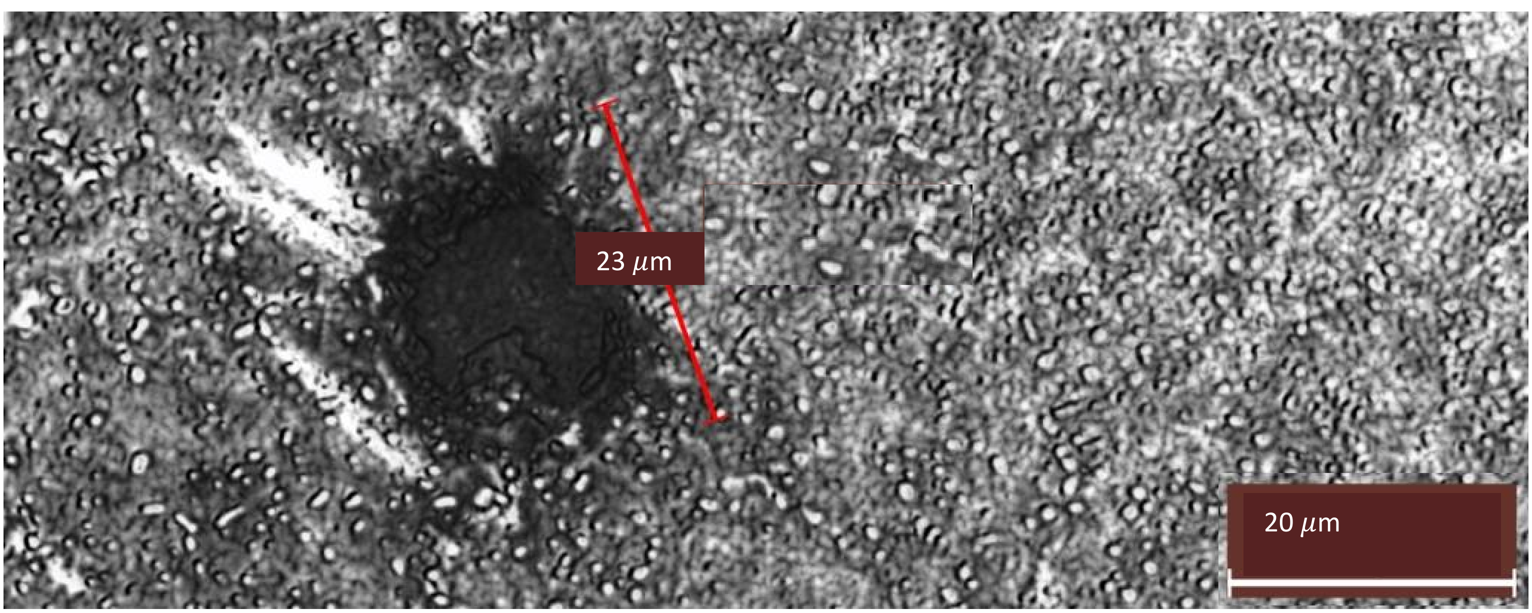

Figure 6.5-butterfly wings being formed only at one end of inclusion. also, the inclusion is not well attached to the surrounding steel matrice-tested 17.7 hours

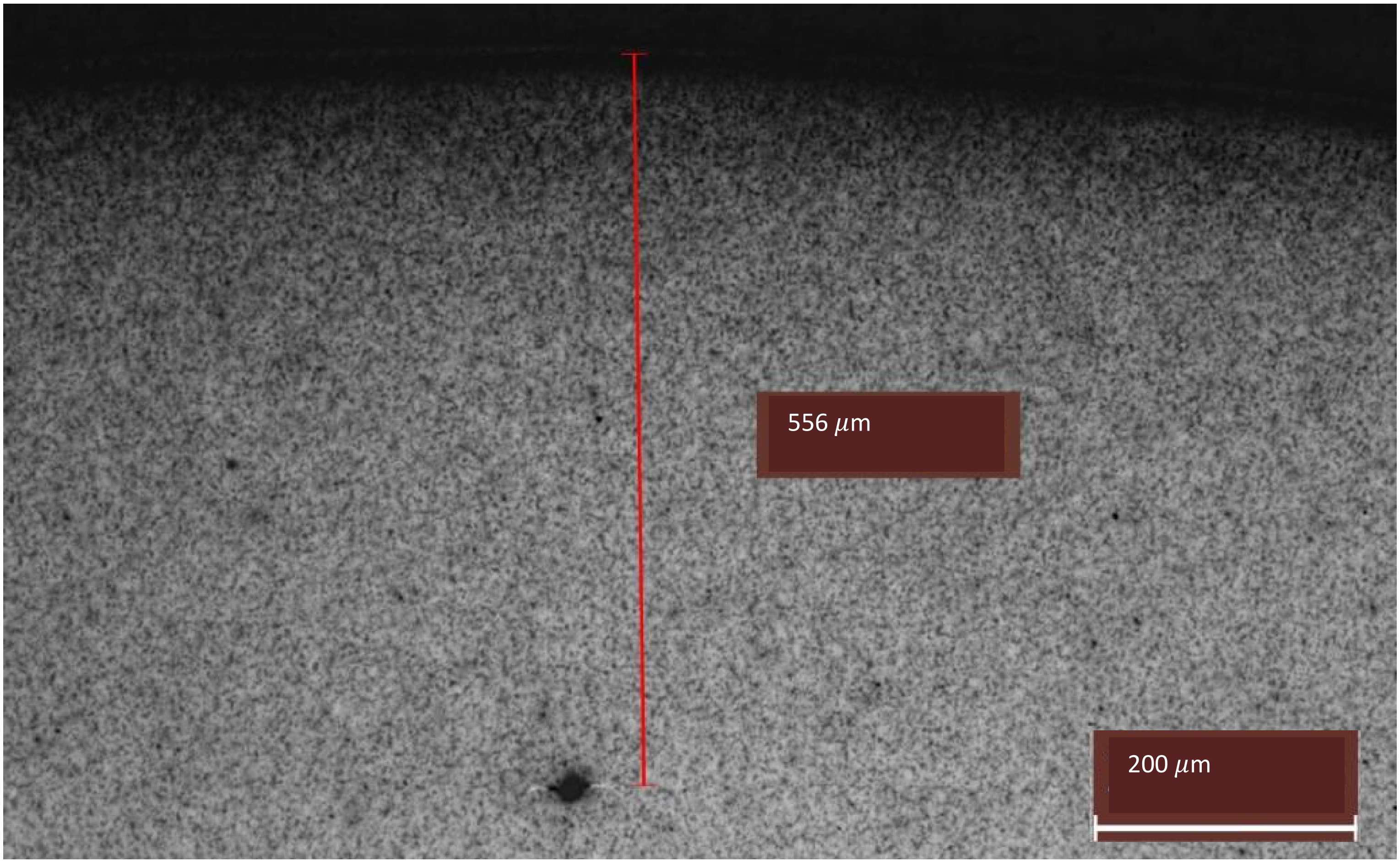

Figure 6.6crack nucleation around an inclusion and formation of butterfly after 20.7 hours

although most of the initiation of cracks observed was due to presence of inclusion, in figure 6.7 we can see crack formation in a region without any inclusion.

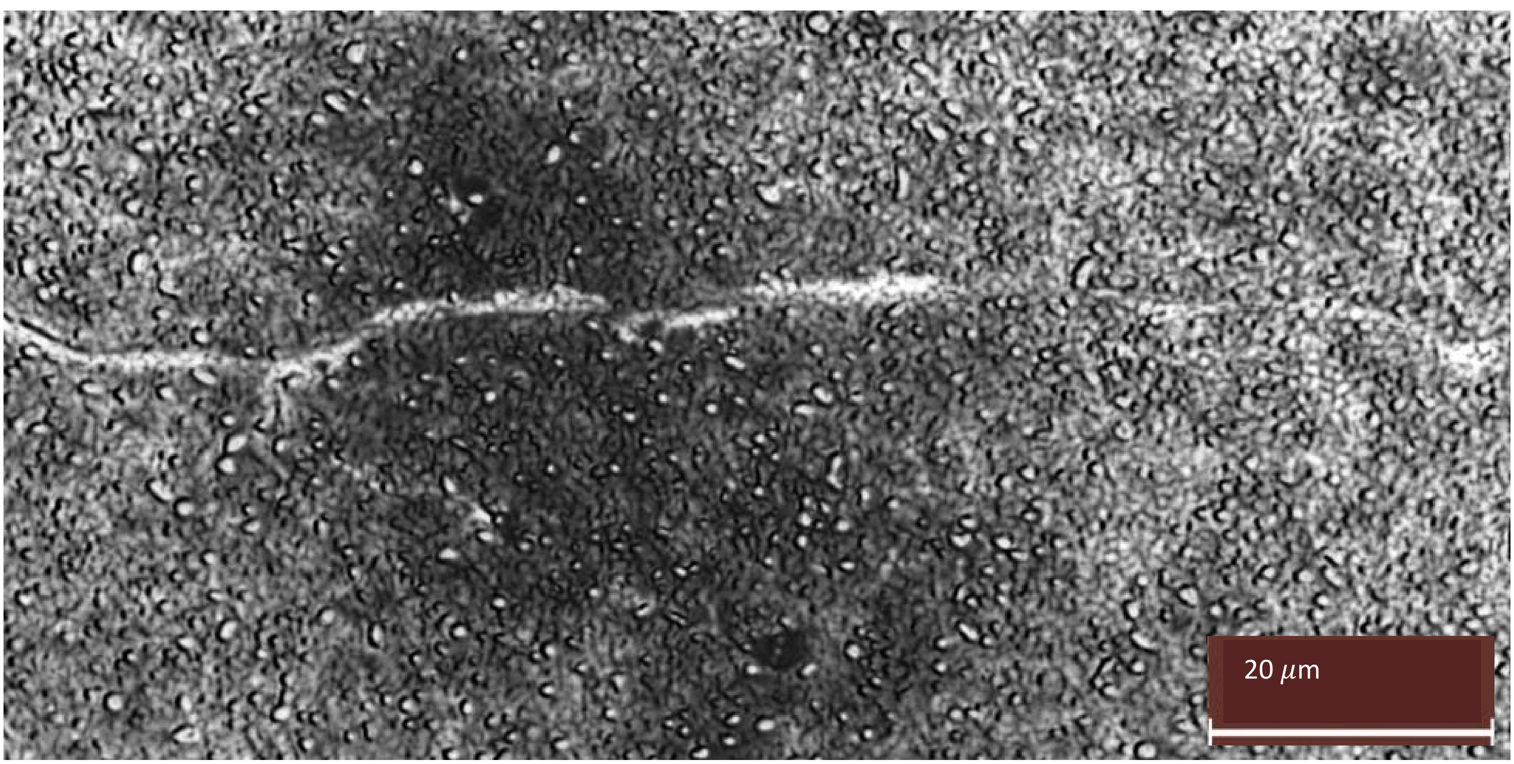

Figure 6.7-although the crack formation can be seen no presence of inclusion was observed. Observation after 29.4h of test

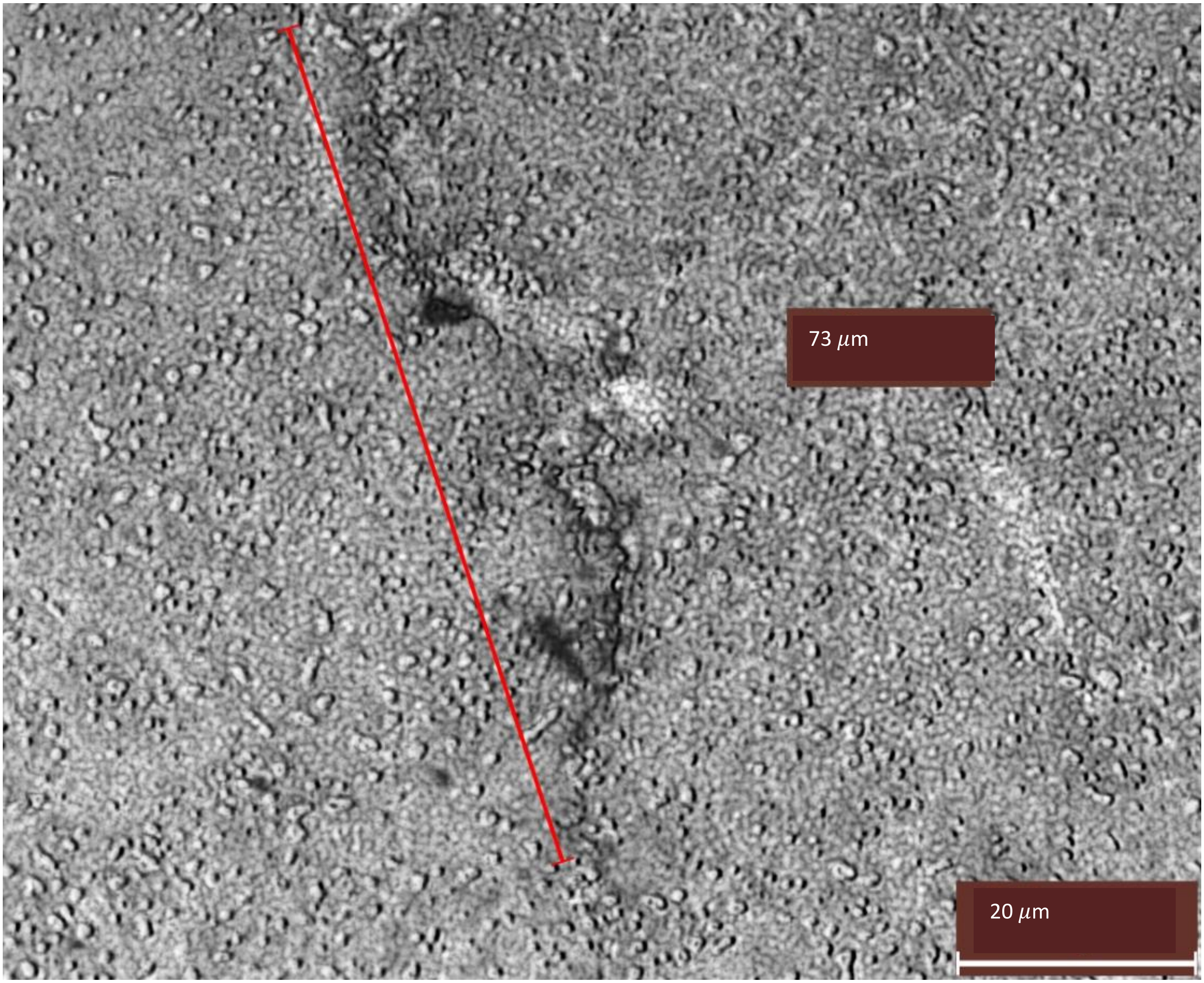

Figure 6.8- the propagation of crack around an inclusion was observed which was tested for 54.1h. Also, we can see the formation of white etching bands in one side of crack.

In figure 6.9 we can see the formation of white etching cracks. Although there are many visible microstructural alterations, but the initiation is occurring around an inclusion.

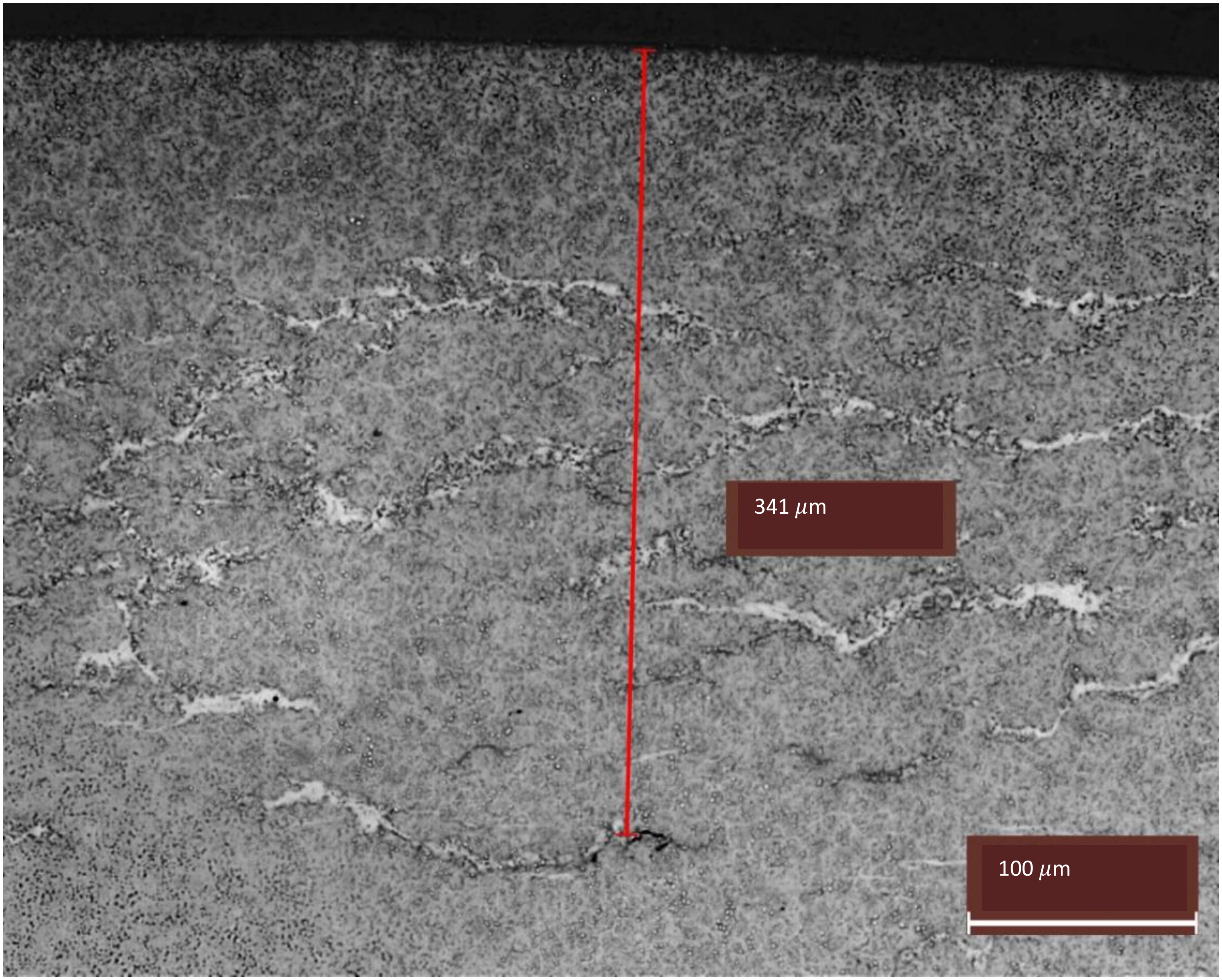

Figure 6.9-formation of white etching cracks. Tested for 92.4 hours

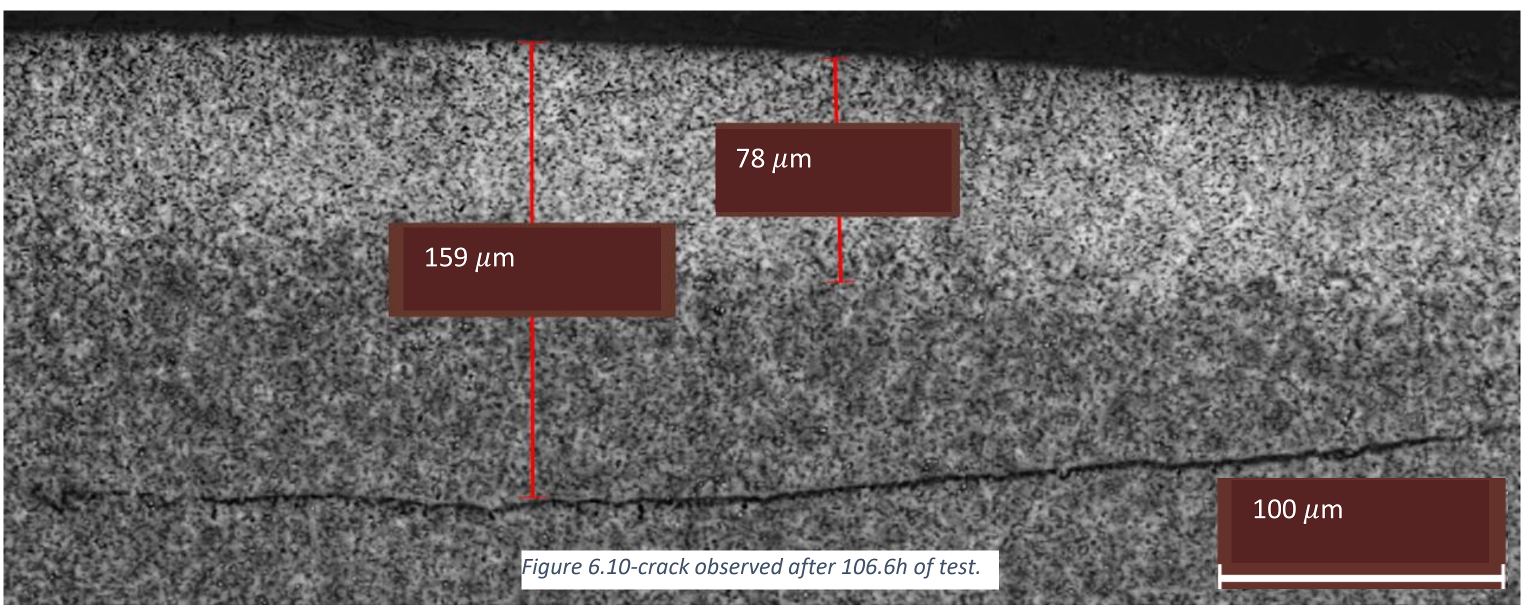

Figure 6.10-crack observed after 106.6h of test.

In order to understand what the difference of the hardness of white etching bands and the surrounding steel is some tests were performed to measure Vickers hardness. Since the area is so small the smallest force increment was implemented by the instrument in order to avoid producing a large impact. For this calculation the simple formula of Vickers was used: $Hv = \frac{1.854f}{d^2} \left[kgf \ / \ mm^2 \right]$

Where 0.01 kgf was used by instrument to create impact.

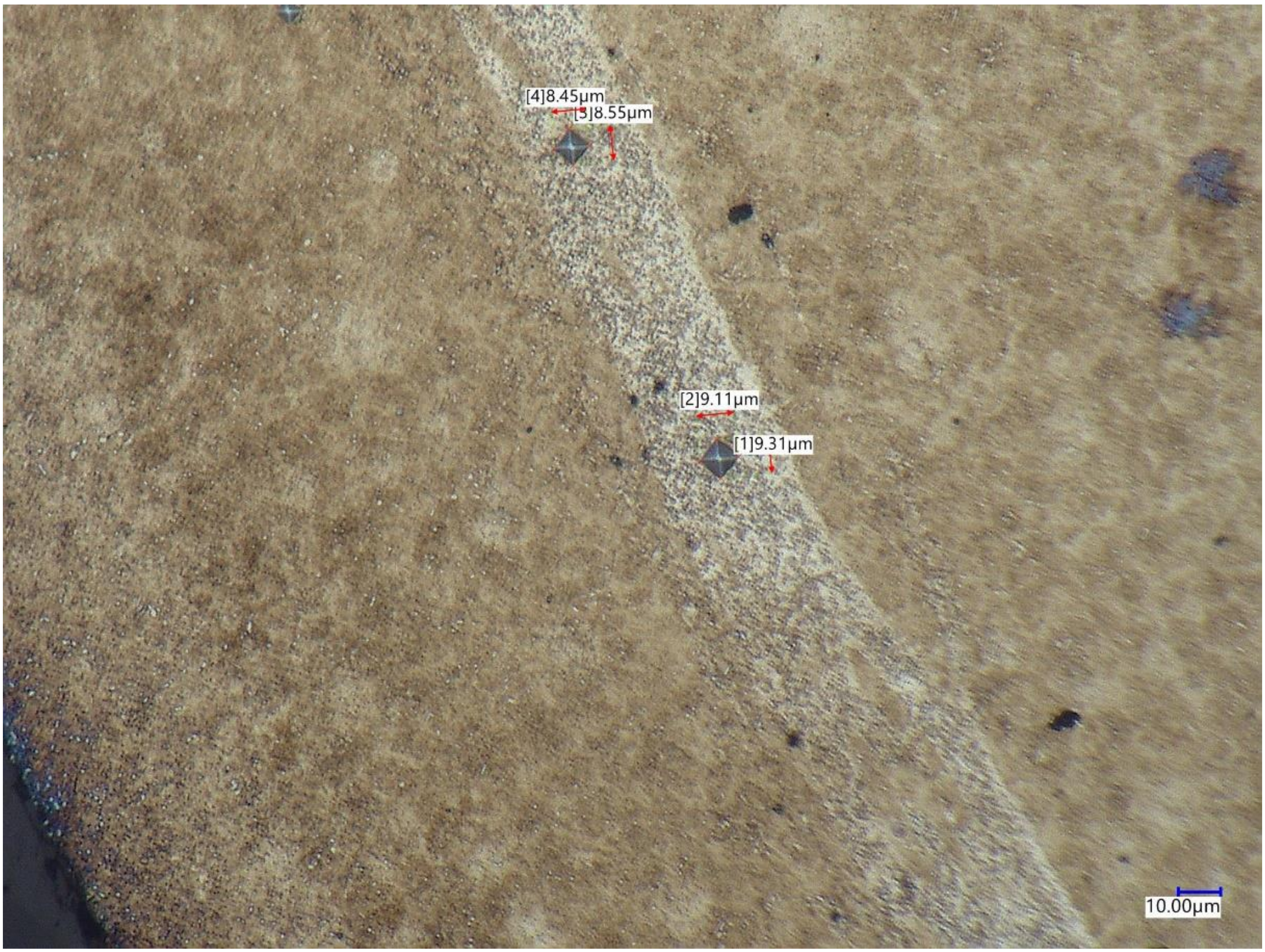

Figure 6.11-micro-hardness test

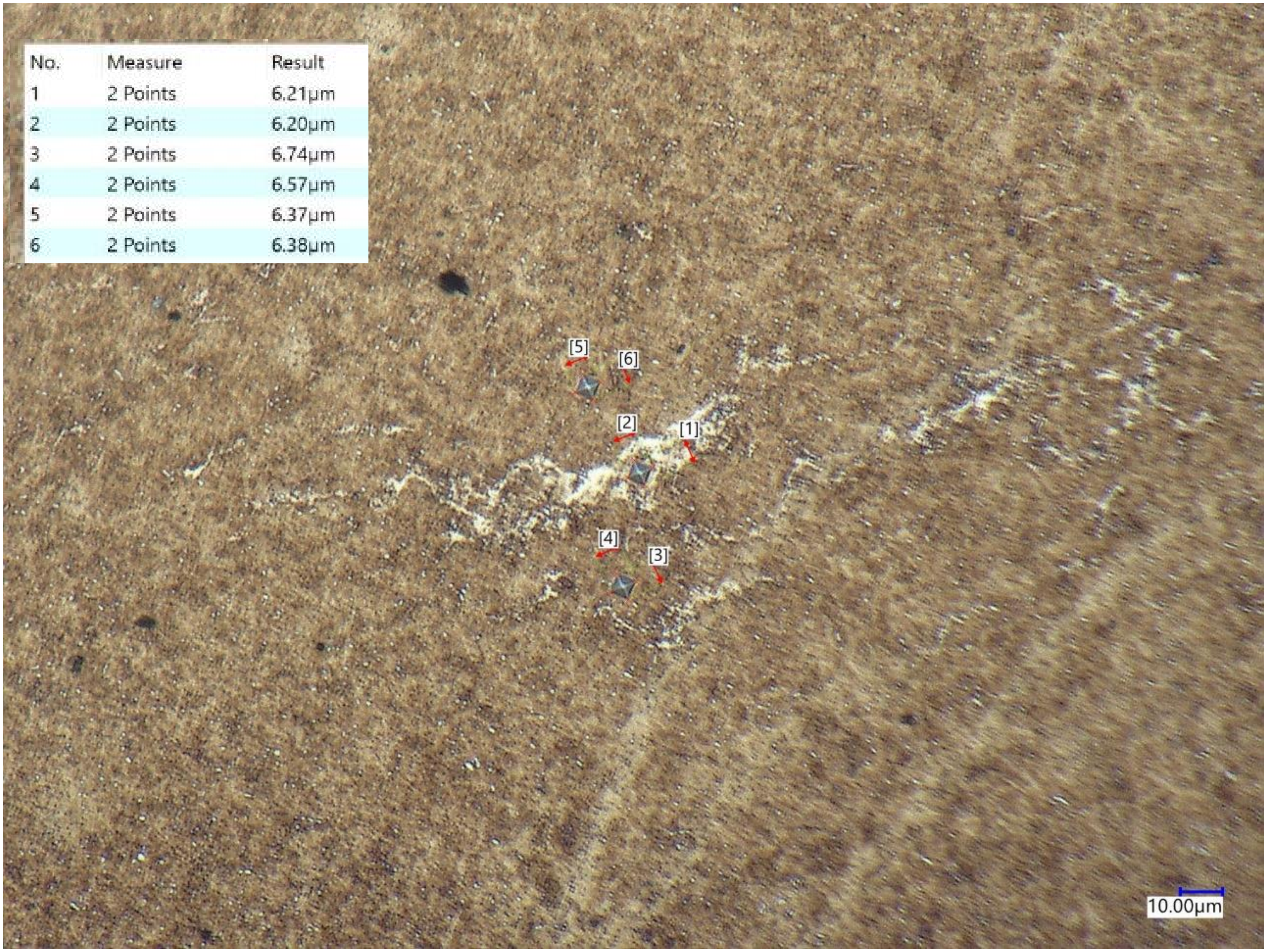

Figure 6.12-micro-hardness test2

Table 6.2 micro-hardness measurements of matrice and WEB

PIC Name	D1(micron)	D2(micron)	D-Avg(millimeter)	Vickers hardness
1_matrice	**6.57**	**6.75**	**0.00666**	**417.9855531**
2-matrice	**7.09**	**7.08**	**0.007085**	**369.343126**
3-matrice	**7.2**	**6.93**	**0.007065**	**371.4372005**
1-WEB(Dim. 1&2)	**8.39**	**8.38**	**0.008385**	**263.6960327**
1-WEB(Dim. 3&4)	**7.63**	**8.04**	**0.007835**	**302.0172357**
2-WEB	**7.32**	**7.27**	**0.007295**	**348.3847509**
3-WEB(Dim. 1&2)	**9.31**	**9.11**	**0.00921**	**218.5699583**
3-WEB(Dim. 3&4)	**8.55**	**8.45**	**0.0085**	**256.6089965**
4-matrice	**6.01**	**6.06**	**0.006035**	**509.0438336**
5-matrice	**6.28**	**6.49**	**0.006385**	**454.765936**
4-WEB	**8.15**	**8.1**	**0.008125**	**280.8426036**
5-WEB(Dim. 1&2)	**7.77**	**7.65**	**0.00771**	**311.8896577**
5-WEB(Dim. 3&4)	**7.68**	**7.55**	**0.007615**	**319.7200811**
		average WEB hardness =		**287.7161646**
		average matrice hardness =		**437.7846122**

As we can see from the results a significant decrease in the matrice hardness can be observed after formation of white etching bands.

The calculated average depth is in the vicinity of the maximum shear stress depth for the Hertzian contact pressure corresponding to 34,4 *KN* force applied on tests.

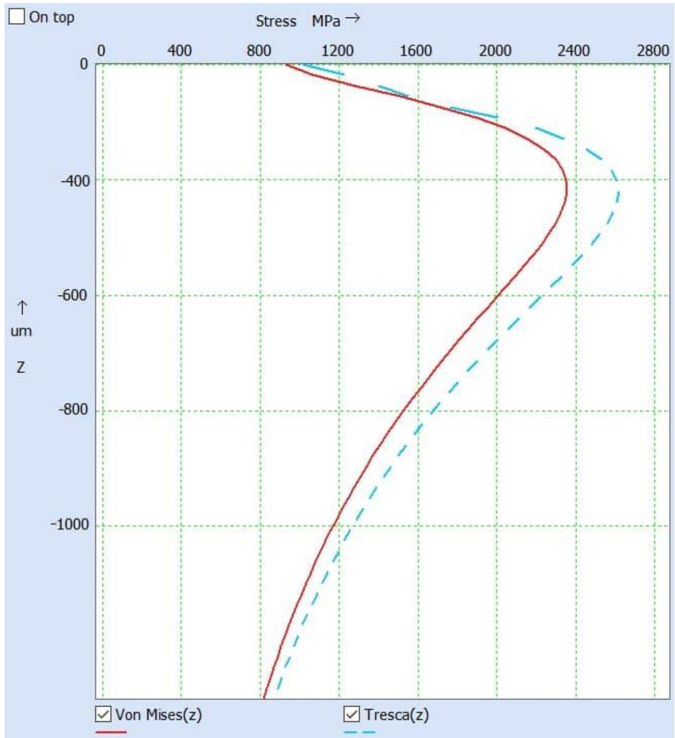

Figure 6.13-subsurface contact stresses for 34.4 KN for 11.112

Since the failures was happened in different life span of fatigue life, the scattered data gathered for the failure time was not so useful in order to understand when the fracture is happening.

Figure 6.14 failed ball after 34.2 h of test depth of crack=-436

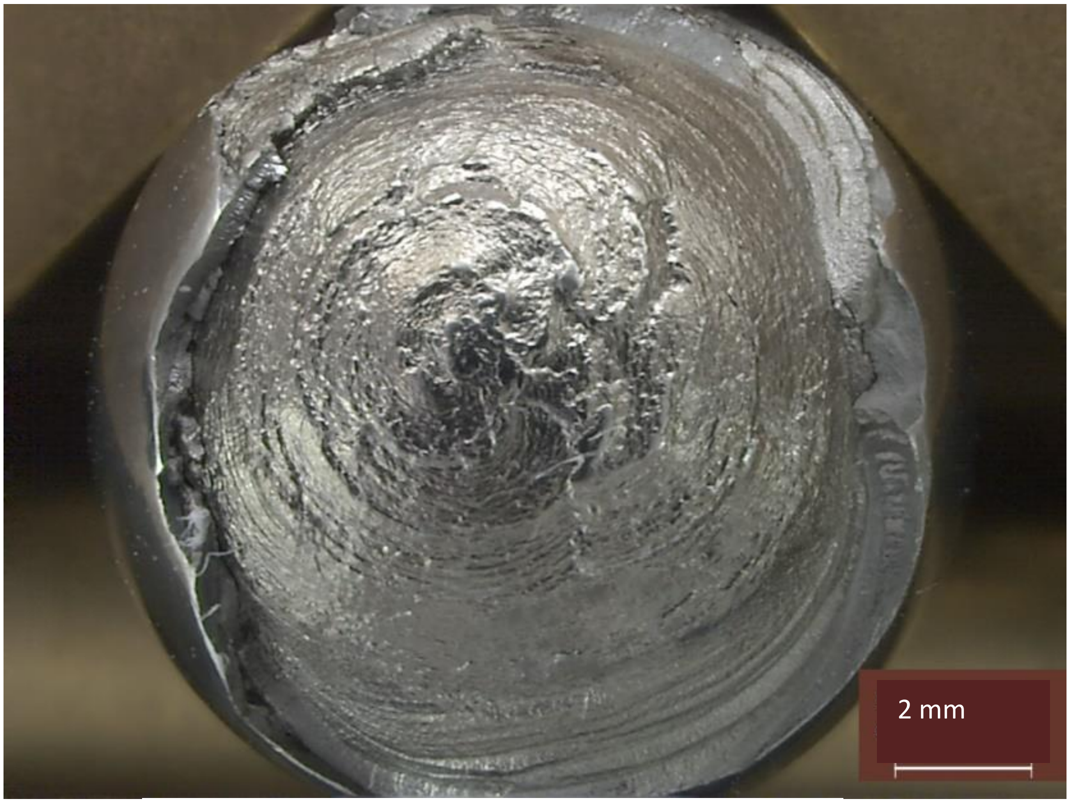

Figure 6.15-inclusion initiated failure after 54.1 h of test at depth=-576

from measurements on the new balls (not tested) the average value for residual stress on new balls are obtained. The data on legend indicates different lots of new balls.

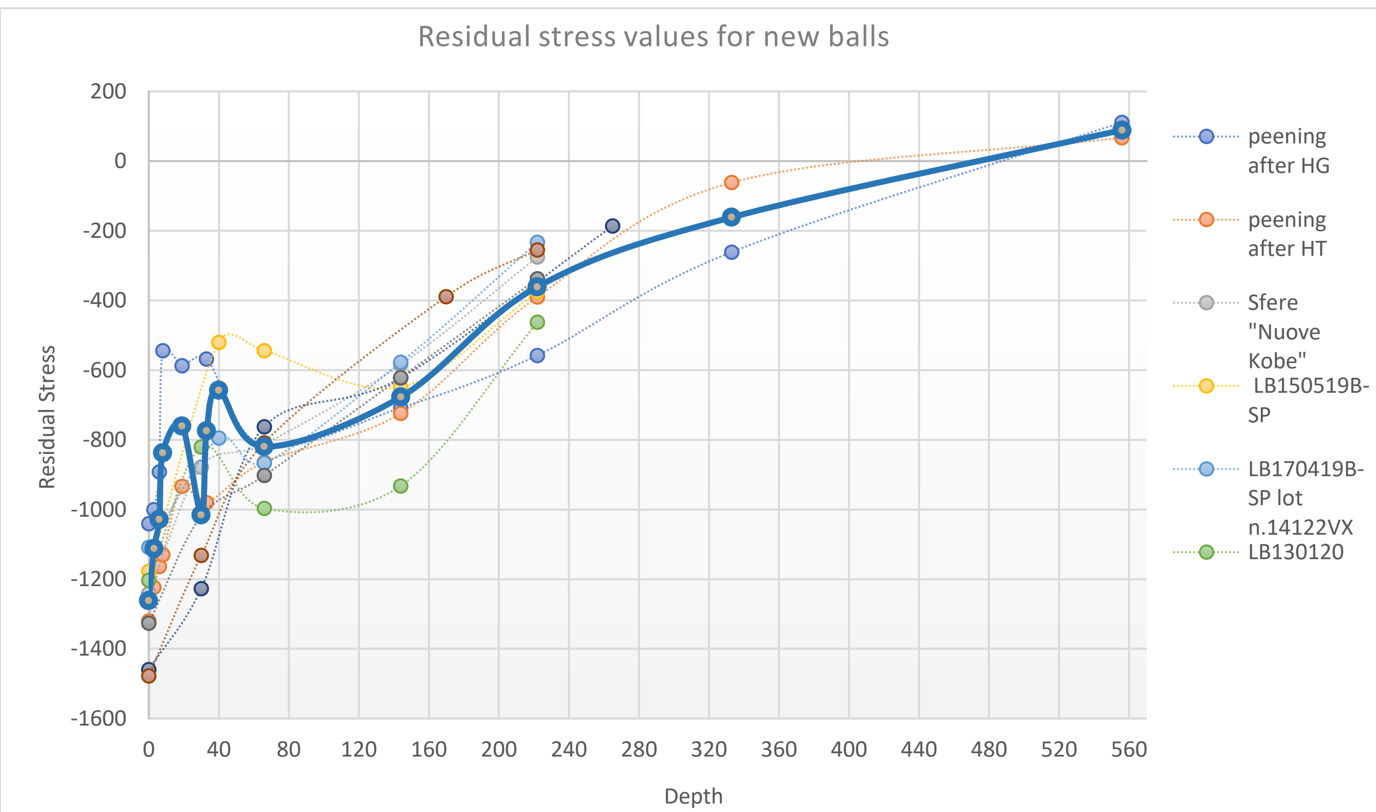

Figure 6.16 average value of residual stress for different new balls

The value of residual stress is calculated for the survived balls from the stopped test. (notice that on each test 7 balls are mounted, and the test usually stops when one of the balls fail inside the bearing). Then in order to understand the changes that undergoes at critical depth, which is the maximum shear stress depth, the gathered data are sorted according to each depth which lead to some interesting results.

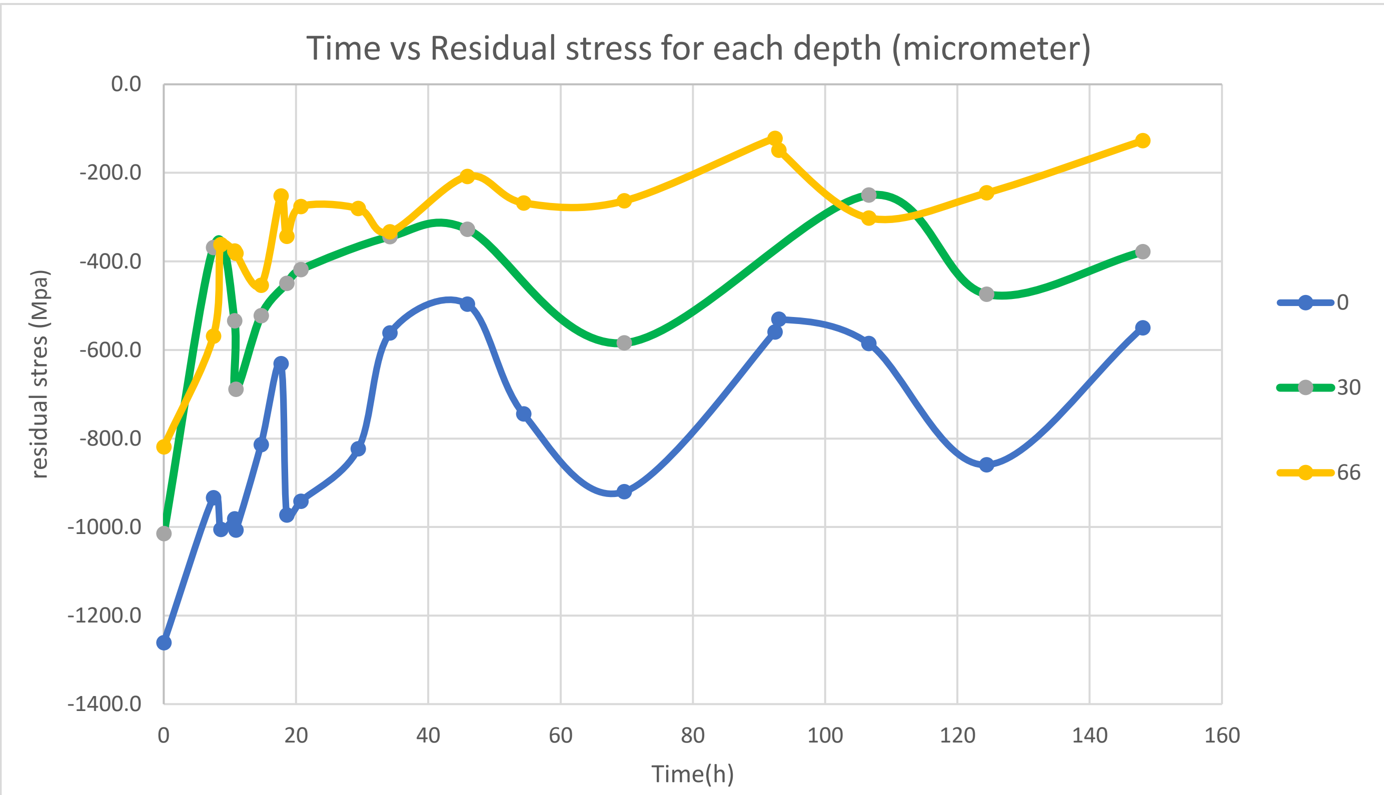

Figure 6.17 value of residual stress at each time frame for shalow depths of micrometer

The value of residual stress has been decreased sharply after around 10 hours of test in the depths. If we look at the related depths we can see that this decrease is happening where we can see the dark etching region in the material and also the decrease in the value of retained austenite which tell us the expansion of material due to transformation to martensite and since the martensite lattice has larger volume this expansion is leading to a decrease in residual stress value.

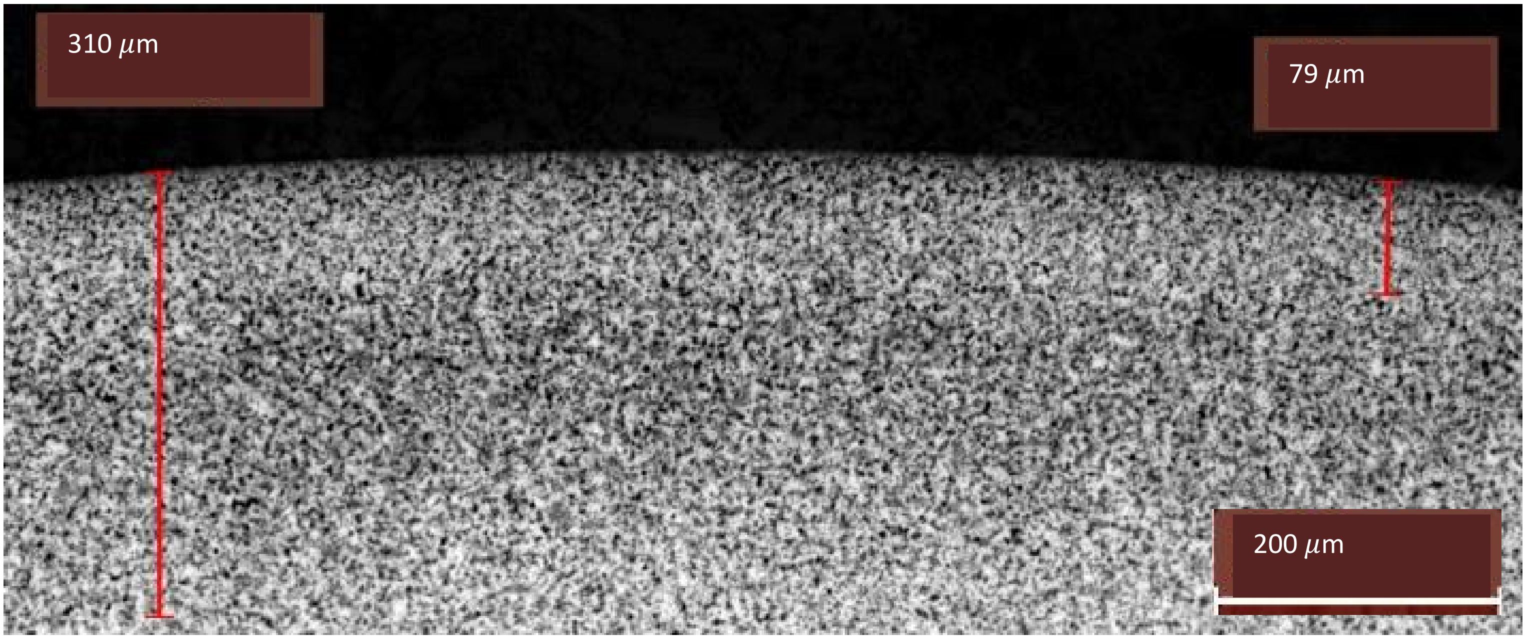

the residual stress values for depths which are in the vicinity of maximum shear stress are experiencing a sharp increase in their early stage of life which can add a significant contribution when we consider this value to the Eshelby solution. The increase of residual stress in this region can be justified by the expansion of the upper part (dark etching area).

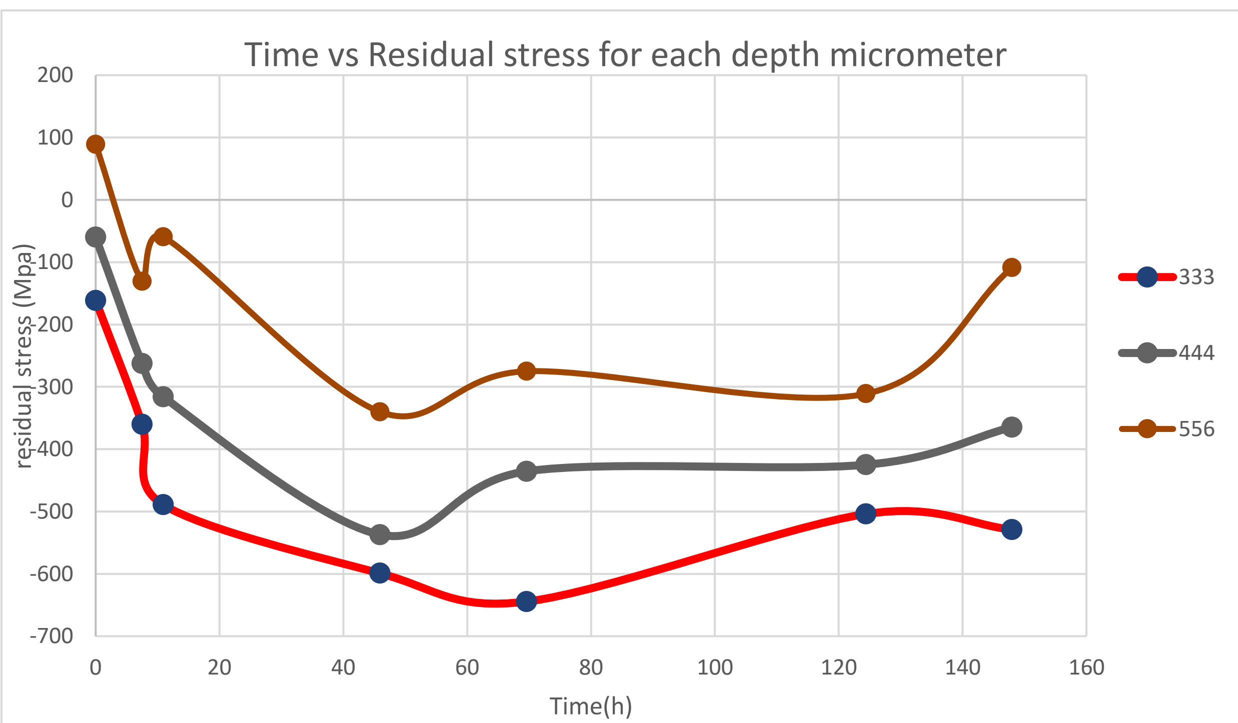

Figure 6.19 the value of residual stress around critical depth (micrometer)

by adding the contribution of increased residual stress, we can see an increase of 15% in the value of Tresca stress. In figure 7.8 the 300-400 Mpa increase in stress state due to increase of residual stresses which was observed in figure 7.7 was assumed to be in radial direction and then it was added to the stress-vector matrix in MATLAB code in order to simulate the increased increment of stress due to residual stress changes.

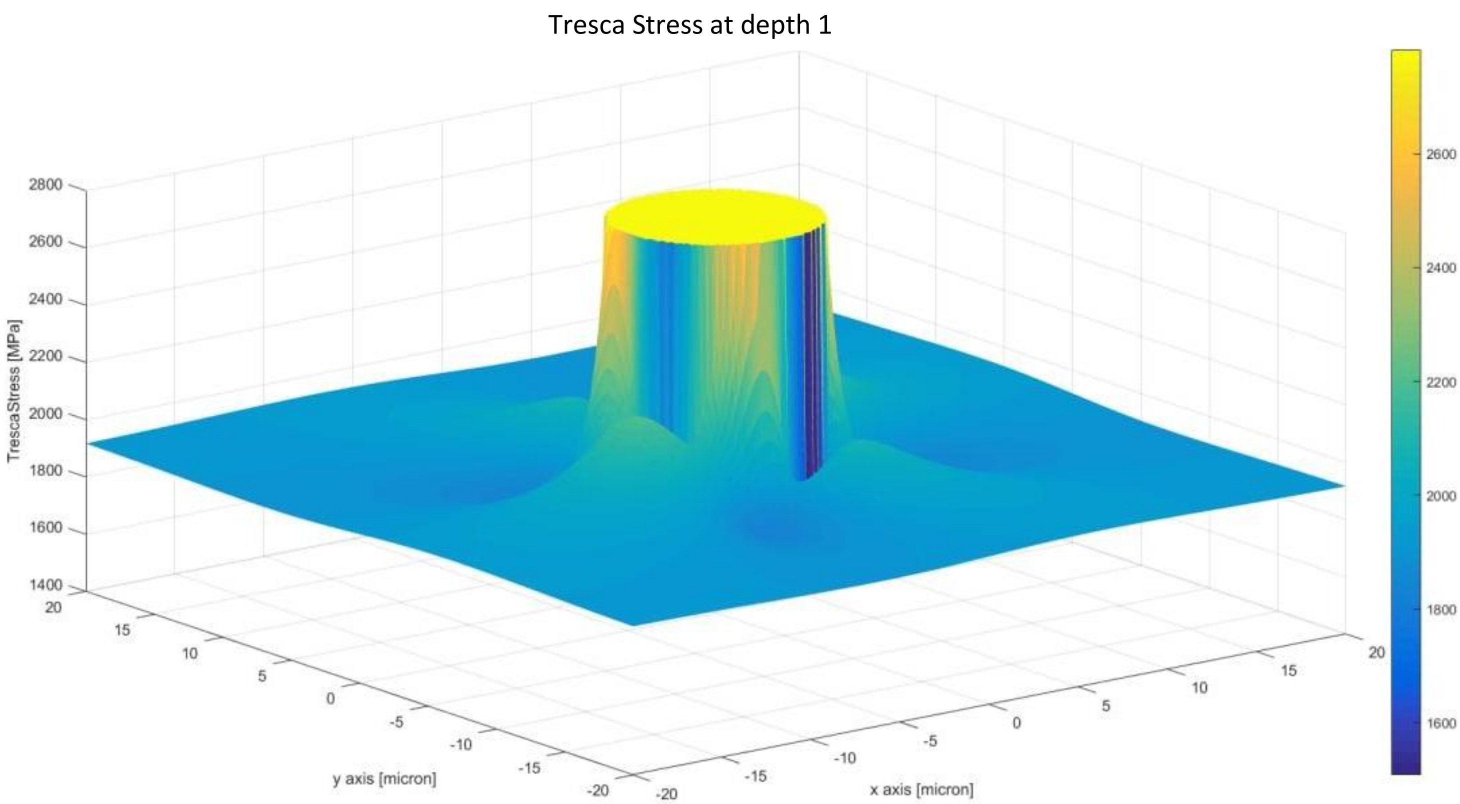

Figure 6.20 Maximum shear stress considering the residual drop

7.Conclusion

The main target of this study was to evaluate the influence of residual stress and micro-inclusions on crack initiation and fatigue life of bearings. In order to do so the effect of increase in compressive residual stresses in maximum shear stress depth and decrease in shallower depth on the stress field of 100Cr6 balls was studied. The tests on balls were performed on Test Rigs and Residual stress measurements could be done thanks to Xray diffractometer. The fracture depth could be assessed by a gauge-meter scanning electron microscope and optical microscope.

The stress state was evaluated in a condition which the initial increase in residual stress state was added to the stress state with inclusion. This study can be a good explanation for why presence of inclusion in regions that are in a certain depth are critical and what happens to the stress state around inclusion during time. In order to see the microstructural alterations at times which were the initiation time of crack several balls were cut and etched and the observed changes were related to expectations. In order to understand the micro-hardness of WEB micro-Vickers test measurement was performed and showed the decrease of hardness happens by formation of WEB

8.Future works

Although the results obtained were satisfactory further investigation could be made in order to find the 3D residual stress state in balls. Also, the effect of cyclic hardening and plastic strain cumulation should be studied in order to better understanding of shakedown process in rolling contact. Also, the presence of two inclusions in vicinity of each other and the effect of presence of such cases in increase in the stress field is of great importance. Regarding the numerical model an optimization could be implemented to find the best initial stress state for the new balls.

Reference:

[1] Bhadeshia H K D H 2012 Steels for bearings *Prog. Mater. Sci.* **57** 268–435

[2] Hashimoto K, Fujimatsu T, Tsunekage N, Hiraoka K, Kida K and Santos E C 2011 Study of rolling contact fatigue of bearing steels in relation to various oxide inclusions *Mater. Des.* **32** 1605–11

[3] A. B. Jones 1947 METALLOGRAPHIC OBSERVATIONS OF BALL BEARING FATIGUE PHENOMENA

[4] Sadeghi F, Jalalahmadi B, Slack T S, Raje N and Arakere N K 2009 A Review of Microstructural Alterations around Nonmetallic Inclusions in Bearing Steel during Rolling Contact Fatigue *J. Tribol.* **131** 1–15

[5] Furumura K, Murakami Y and Abe T 1993 The Development of Long Life Bearing Steel for Full Film Lubrication and for Poor and Contaminated Lubrication *Astm* 199–210

[6] Moghaddam S M and Sadeghi F 2016 A Review of Microstructural Alterations around Nonmetallic Inclusions in Bearing Steel during Rolling Contact Fatigue *Tribol. Trans.* **59** 1142–56

[7] Becker P C 1981 Microstructural changes around non-metallic inclusions caused by rolling-contact fatigue of ball-bearing steels *Met. Technol.* **8** 234–43

[8] Zwirlein O and Schlicht H 1982 Rolling contact fatigue mechanisms - accelerated testing versus field performance. *Roll. Contact Fatigue Test.*

Bear. Steels Symp., (Phoenix, U.S.a. May 12-14, 1981), J.J.C. Hoo (Astm Publ. 358–79

[9] Ruellan A, Ville F, Kleber X, Arnaudon A and Girodin D 2014 Understanding white etching cracks in rolling element bearings: The effect of hydrogen charging on the formation mechanisms *Proc. Inst. Mech. Eng. Part J J. Eng. Tribol.* **228** 1252–65

[10] Stiénon A, Fazekas A, Buffière J Y, Vincent A, Daguier P and Merchi F 2009 A new methodology based on X-ray micro-tomography to estimate stress concentrations around inclusions in high strength steels *Mater. Sci. Eng. A* **513–514** 376–83

[11] Fu H, Rydel J J, M.Gola A, Yu F, Geng K, Lau G, Luo H, E.J P and Rivera-Diaz-del-Castillo 2019 The relationship between 100Cr6 steelma...nd rolling contact fatigue performance.pdf 10

[12] Grabulov A, Petrov R and Zandbergen H W 2010 EBSD investigation of the crack initiation and TEM/FIB analyses of the microstructural changes around the cracks formed under Rolling Contact Fatigue (RCF) *Int. J. Fatigue* **32** 576–83

[13] Mahdavi H, Poulios K and Niordson C F 2020 Effect of superimposed compressive stresses on rolling contact fatigue initiation at hard and soft inclusions *Int. J. Fatigue* **134** 105399

[14] Taylor P, Liu J Y, Tallian T E and Mccool J I 2008 Dependence of Bearing Fatigue Life on Film Thickness to Surface Roughness Ratio Dependence of Bearing Fatigue Life on Film Thickness to Surface Roughness Ratio 37–41

[15] Moghaddam S M 2015 Butterfly Wing Formation In Bearing Steel

[16] Harris T A, Ragen M A and Spitzer R F 1992 The effect of hoop and material residual stresses on the fatigue life of high speed, rolling bearings *Tribol. Trans.* **35** 194–8

[17] Coelho L, Dias A, Lieurade H P and Maitournam H 2004 Experimental and numerical rolling contact fatigue study on the 32CrMoV13 steel *Fatigue Fract. Eng. Mater. Struct.* **27** 811–23

[18] Bower A F and Johnson K L 1991 Plastic flow and shakedown of the rail surface in repeated wheel-rail contact *Wear* **144** 1–18

[19] Voskamp A P 1985 Material response to rolling contact loading *J. Tribol.* **107** 359–64

[20] Gili S 2020 POLITECNICO DI TORINO Department of Engineering Master Degree in Mechanical Engineering Effect of non metallic inclusions on the fatigue life of ball bearing Candidate :

[21] Michel B 1989 Mura, T., Micromechanics of Defects in Solids. Second, revised edition. Dordrecht etc., Martinus Nijhoff Publishers 1987. XIII, 587 pp., US $ 162. – /Dfl. 345.-. ISBN 90-247-3343-X (Mechanics of Elastic and Inelastic Solids 3) *ZAMM - J. Appl. Math. Mech. / Zeitschrift für Angew. Math. und Mech.*

[22] Meng C, Heltsley W and Pollard D D 2012 Evaluation of the Eshelby solution for the ellipsoidal inclusion and heterogeneity *Comput. Geosci.* **40** 40–8

[23] Raszillier V 1972 Cation of Material and Hertzian Contact Area Induced *Aerospace* **19** 1–15

[24] Kang J-H, Hosseinkhani B and Rivera-Díaz-del-Castillo P E J 2012 Rolling contact fatigue in bearings: multiscale overview *Mater. Sci. Technol.* **28** 44–9

[25] Muzio M. Gola 2015 Hertz contacts & bearings

[26] Johnson K L 1989 Contact Mechanics

[27] Edited E *Materials Research and Engineering Edited by B. llschner and N. 1. Grant*

Websites:

1. https://en.wikipedia.org/wiki/Bragg%27s_law
2. https://github.com/Chunfang/Esh3D

List of figures

Appendix

Profiles of residual stresses

Residual measurements of the balls tested on the test rigs

	Depth=0	Depth=20	depth=30	depth=66	depth=144	depth=222	depth=333	depth=444	depth=556
Time	Residual stress								
0	-1261.5	-760.25	-1015	-819.4444444	-677	-360.75	-161.25	-60	89.25
7.5	-934	-436	-369	-569	-509	-536.5	-360	-262.5	-130.5
8.6	-1005.5	nan		-362.5	-581	-688			
10.7	-981.5	nan	-534.5	-376.5	-599	-748			
10.9	-1007	-701	-689	-382	-481	-533.5	-489	-316	-59.5
14.7	-814		-522.5	-454	-747.5	-830.5			
17.7	-631.5			-252.5	-400.5	-624.5			
18.6	-973		-450	-343.5	-456	-646			
20.7	-942		-419	-277	-541	-667			
29.4	-823.5			-280.5	-563.5	-670			
34.2	-562		-344	-334	-634	-696			
45.9	-497	-524.5	-327.5	-208	-538	-637	-599	-537	-340
54.4	-745			-268	-452	-619.5			
69.6	-920.5	-621.5	-584.5	-263.5	-505.5	-526	-644.5	-435.5	-275
92.4	-559.5			-122	-307.5	-556			
93	-530.5			-149	-404	-608			
106.6	-586		-251	-302	-578	-686			
124.4	-859.5	-545.5	-474	-245.5	-567.5	-554	-504	-425	-311
148	-550	-382	-378.5	-127.5	-203.5	-479.5	-529	-364.5	-108.5

Residual stress vs depth profiles of balls for all the tests.

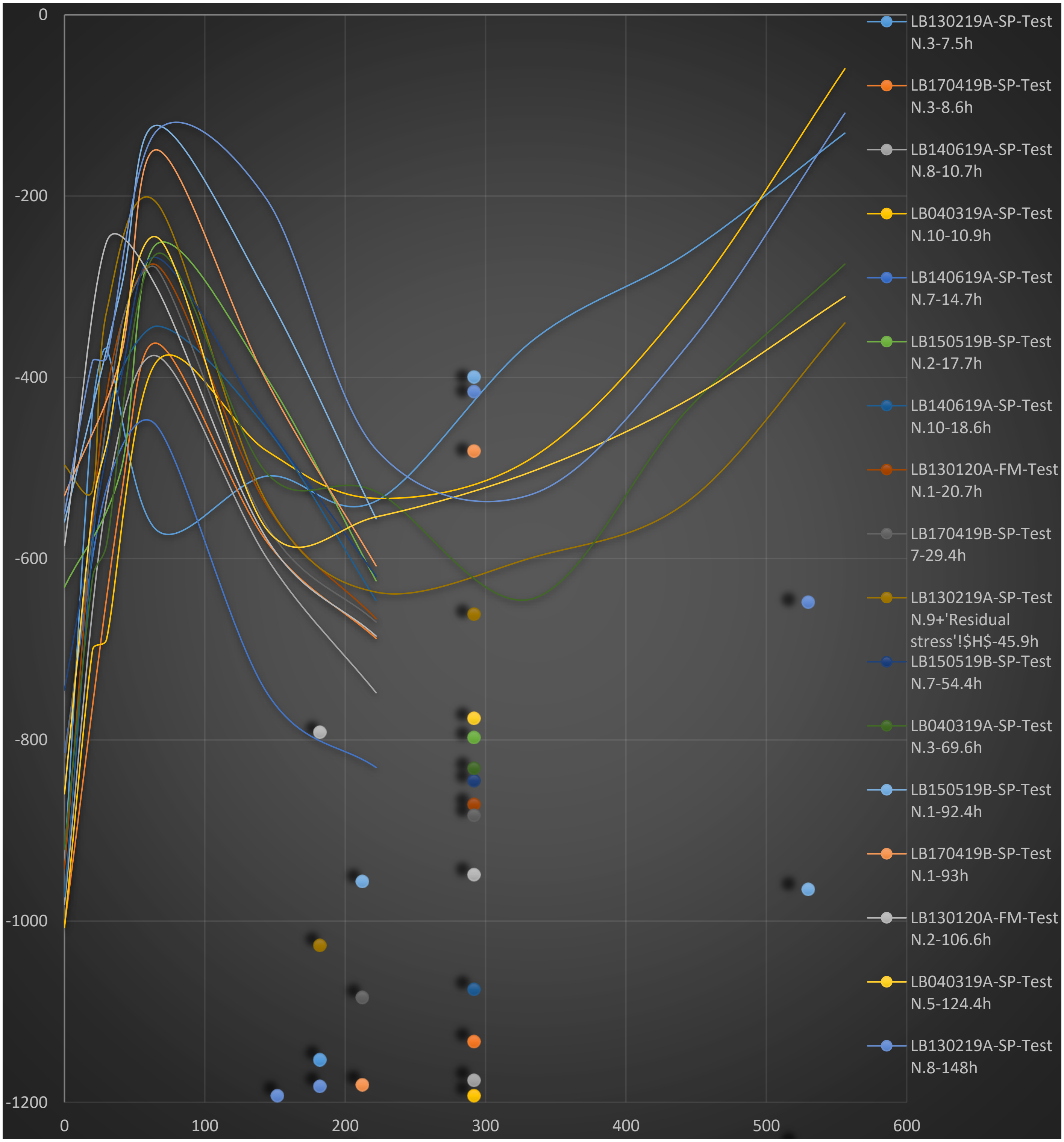

Some of unusual failures observed after test. Depth of failure in these cases are significantly smaller than expected

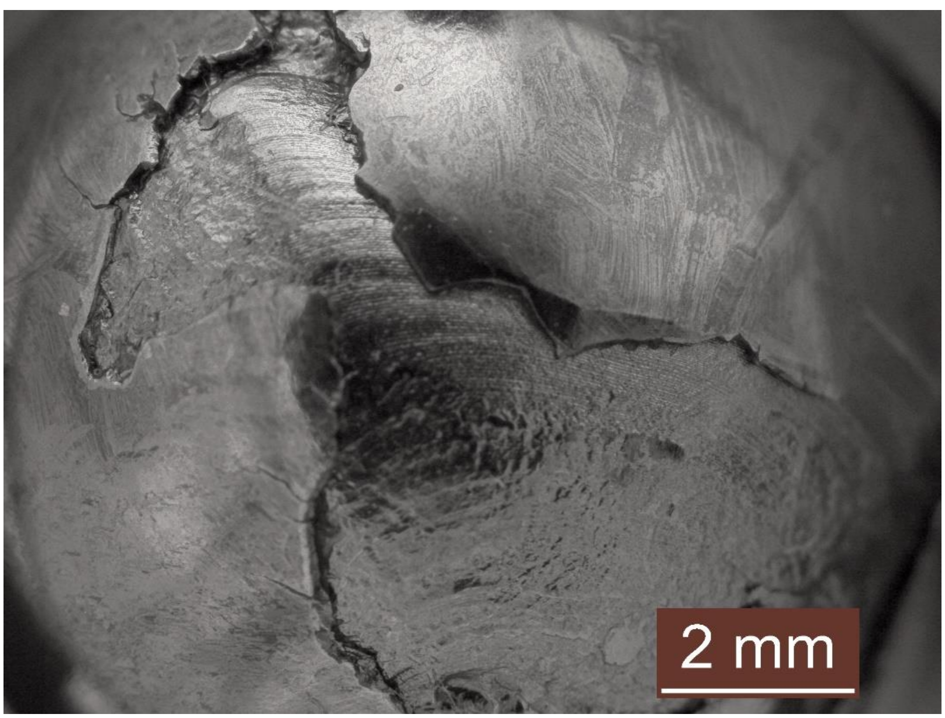

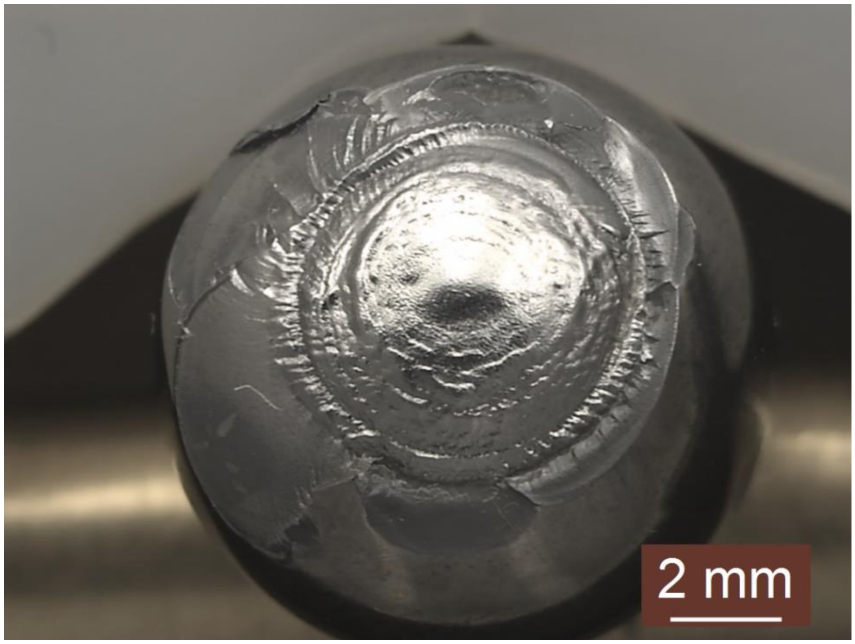

other usual fractures

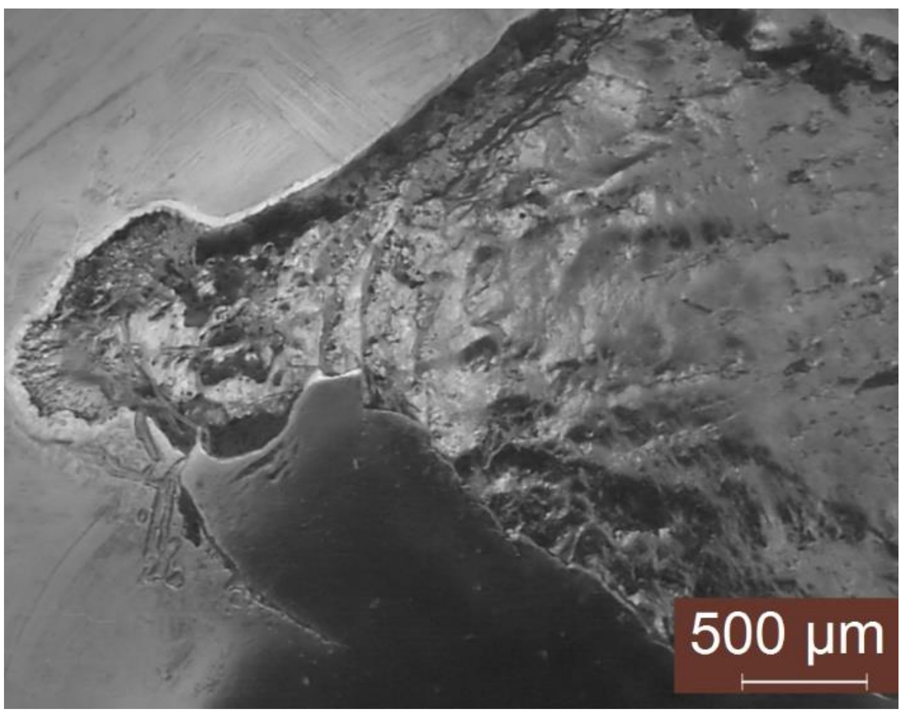

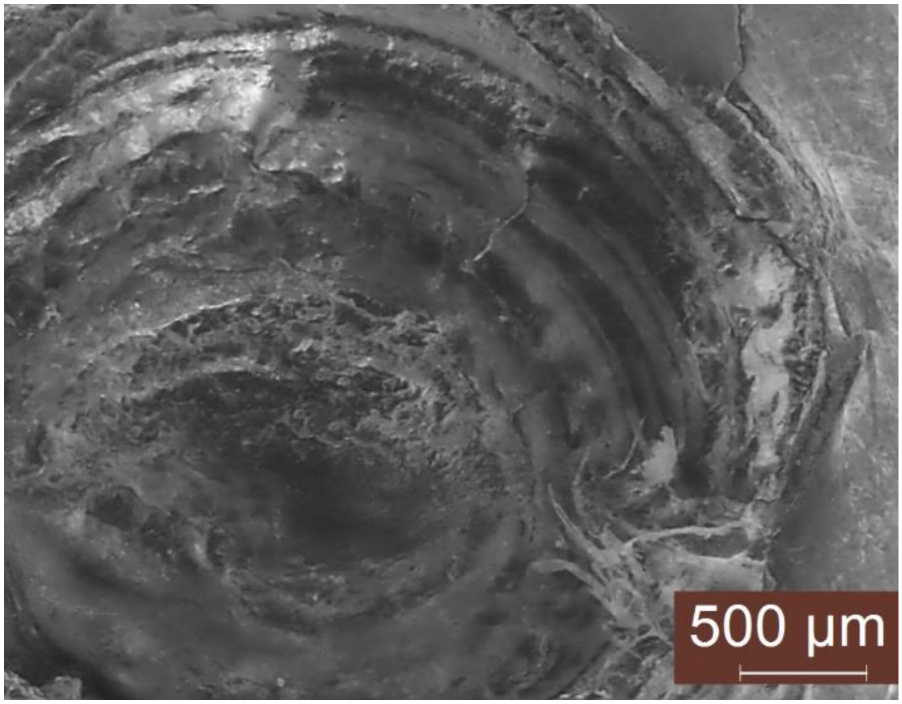
500 µm

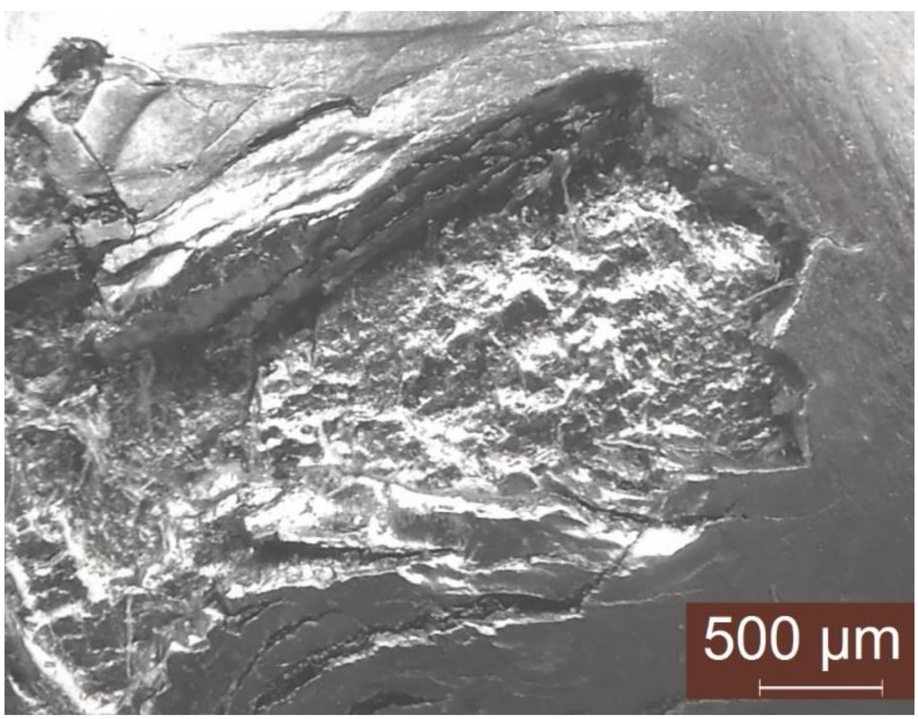
500 µm